Nucleon axial form factor from elementary target data

A. S. Meyer,[1,*] T. Cai,[2,3] M. Moore,[3,†] S. Akhter,[4] Z. Ahmad Dar,[5,4] M. Sajjad Athar,[4] M. Betancourt,[6] H. Budd,[3] G. Caceres,[7,‡] D. S. Correia,[7] G. A. Díaz,[6,3] J. Felix,[8] A. M. Gago,[9] H. Gallagher,[10] P. K. Gaur,[4] S. M. Gilligan,[11] R. Gran,[12] E. Granados,[8,8] D. A. Harris,[2,6] A. L. Hart,[13] R. J. Hill,[14,6] J. Kleykamp,[3,§] A. Klustová,[15] M. Kordosky,[5] D. Last,[3,16] A. Lozano,[7,‖] S. Manly,[3] W. A. Mann,[10] K. S. McFarland,[3] O. Moreno,[5,8] J. K. Nelson,[5] A. Olivier,[17,3,¶] V. Paolone,[18] G. N. Perdue,[6,3] C. Pernas,[5] M. A. Ramírez,[16,8] R. D. Ransome,[19] D. Ruterbories,[3] H. Schellman,[11] C. J. Solano Salinas,[20] N. H. Vaughan,[11] M. O. Wascko,[21,15] and L. Zazueta[5,**]

(MINERvA Collaboration)

[1]*Nuclear and Chemical Sciences Division, Lawrence Livermore National Laboratory, Livermore, California 94550, USA*
[2]*York University, Department of Physics and Astronomy, Toronto, Ontario, M3J 1P3 Canada*
[3]*Department of Physics and Astronomy, University of Rochester, Rochester, New York 14627 USA*
[4]*Department of Physics, Aligarh Muslim University, Aligarh, Uttar Pradesh 202002, India*
[5]*Department of Physics, William & Mary, Williamsburg, Virginia 23187, USA*
[6]*Fermi National Accelerator Laboratory, Batavia, Illinois 60510, USA*
[7]*Centro Brasileiro de Pesquisas Físicas, Rua Dr. Xavier Sigaud 150, Urca, Rio de Janeiro, Rio de Janeiro, 22290-180, Brazil*
[8]*Campus León y Campus Guanajuato, Universidad de Guanajuato, Lascurain de Retana No. 5, Colonia Centro, Guanajuato 36000, Guanajuato México*
[9]*Sección Física, Departamento de Ciencias, Pontificia Universidad Católica del Perú, Apartado 1761, Lima, Perú*
[10]*Physics Department, Tufts University, Medford, Massachusetts 02155, USA*
[11]*Department of Physics, Oregon State University, Corvallis, Oregon 97331, USA*
[12]*Department of Physics, University of Minnesota–Duluth, Duluth, Minnesota 55812, USA*
[13]*G O Jones Building, Queen Mary University of London, 327 Mile End Road, London E1 4NS, United Kingdom*
[14]*Department of Physics and Astronomy, University of Kentucky, Lexington, Kentucky 40506, USA*
[15]*The Blackett Laboratory, Imperial College London, London SW7 2BW, United Kingdom*
[16]*Department of Physics and Astronomy, University of Pennsylvania, Philadelphia, Pennsylvania 19104, USA*
[17]*Department of Physics and Astronomy, University of Notre Dame, Notre Dame, Indiana 46556, USA*
[18]*Department of Physics and Astronomy, University of Pittsburgh, Pittsburgh, Pennsylvania 15260, USA*
[19]*Rutgers, The State University of New Jersey, Piscataway, New Jersey 08854, USA*
[20]*Facultad de Ciencias Físicas, Universidad Nacional Mayor de San Marcos, CP 15081, Lima, Perú*
[21]*Oxford University, Department of Physics, Oxford, OX1 3PJ United Kingdom*

(Received 10 February 2026; accepted 6 August 2026; published 8 September 2026)

Precise neutrino-nucleon amplitudes are essential ingredients for predicting neutrino event rates in current and upcoming long-baseline neutrino oscillation experiments. A common neutrino interaction with a low reaction threshold and with most of the energy carried by two final state particles is quasielastic scattering, for which the nucleon axial form factor, $F_A(Q^2)$, is a dominant source of uncertainty. Improvements to the nucleon axial form factor rely on neutrino scattering data with elementary targets to reduce or eliminate the need for nuclear modeling systematics. This work examines constraints on the

[*]Contact author: meyer54@llnl.gov
[†]Now at SLAC National Accelerator Laboratory and Stanford University Department of Physics, Menlo Park, California 94025, USA.
[‡]Now at Department of Physics and Astronomy, University of California at Davis, Davis, California 95616, USA.
[§]Now at Department of Physics and Astronomy, University of Mississippi, Oxford, Mississipppi 38677.
[‖]Now at Department of Physics, Drexel University, Philadelphia, Pennsylvania 19104, USA.
[¶]Now at Argonne National Laboratory, Lemont, Illinois 60439, USA.
[**]Now at Syracuse University, Syracuse, NY 13244, USA.

Published by the American Physical Society under the terms of the Creative Commons Attribution 4.0 International license. Further distribution of this work must maintain attribution to the author(s) and the published article's title, journal citation, and DOI. Funded by SCOAP[3].

nucleon axial form factor that can be achieved from datasets of neutrino scattering on deuterium targets, Lattice QCD predictions, and from the recent hydrogen target data from the MINERvA Collaboration. Significant tension is found between hydrogen and deuterium target data, suggesting that extractions from deuterium underestimate both the central value and uncertainty of the form factor. Parametrizations for and uncertainties of the nucleon axial form factor using the z expansion are provided.

DOI: 10.1103/ptwr-t73j

I. INTRODUCTION

Explorations of the properties of neutrinos and their flavor oscillation are entering a new era of precision. Current and upcoming flagship long baseline neutrino oscillation experimental programs will measure neutrino interactions with exceptional precision, thereby enabling new insights about the neutrino mass hierarchy and CP violation in the leptonic sector [1–5]. In support of the substantial ongoing experimental efforts, new theoretical guidance is needed to help meet the ambitious precision requirements of next-generation neutrino scattering experiments. With help from improved theory constraints, these experiments can maximize their potential for investigating the physics of neutrinos.

Improving the theoretical description of neutrino-nucleus cross sections is not a simple task. Practical limitations prevent the creation of a neutrino beam that is simultaneously narrowly peaked around a single energy and sufficiently intense for a high-statistics measurement. Modern neutrino oscillation experiments therefore cover a range of energies with several different physical mechanisms at play. To extract a spectrum of neutrino interactions at both a near and far detector, which in turn gives access to the oscillation probability as a function of energy, distributions of neutrinos must be statistically reconstructed under the assumption of a model that encompasses all of the known interaction physics. It is therefore of interest to understand and quantify several neutrino interaction processes over a range of incident energies.

Isolated exclusive interaction channels that have both large cross sections and large uncertainties are the primary targets for theoretical improvements. The most prominent of these is neutrino quasielastic scattering, in which a neutrino scatters off of a quasifree nucleon within a bound nuclear system. Neutrino quasielastic scattering is a primary signal measurement process of long baseline neutrino oscillation experiments and the dominant process at play for small neutrino energies. The weak interactions characteristic of neutrino scattering are sensitive to a nucleon axial current that is not probed by electromagnetic interactions. The axial current interaction is therefore not nearly as well constrained by experimental scattering measurements as the vector current interactions that are a part of the electromagnetic interaction.

Despite being less constrained than the vector form factors, the axial form factor has historically been quoted with very small uncertainties. Those small uncertainties result from the use of the dipole parametrization,

$$F_A(Q^2) = \frac{g_A}{(1 + Q^2/M_A^2)^2}, \tag{1}$$

which has a single free parameter, M_A, the "axial mass." This parametrization has insufficient freedom to describe the set of shapes consistent with theoretical constraints and existing experimental data [6,7]. Reanalysis with neutrino-deuterium scattering data and a form factor with more parametrized freedom revealed that the form factor uncertainty should be at least an order of magnitude larger to accommodate the full range of possible form factor shapes [8]. There is also recent evidence from Monte Carlo tunes suggesting that the tuned neutrino quasielastic cross sections are larger than previous fits for the axial from factor from the deuterium data [9,10]. This evidence appeared simultaneously with first principles calculations of lattice quantum chromodynamics (LQCD), which suggest that the axial form factor is underestimated at large momentum transfer by almost 30% [11,12]. A primary interest is to quantify modern constraints of the nucleon axial form factor accurately and with theoretically robust uncertainties. For this purpose, sources that are free or nearly free nucleon targets are most useful. This includes neutrino-deuterium scattering experimental data analyzed in Ref. [8], which in this work are studied in conjunction with the addition of data from the BEBC neutrino-deuterium experiment [13–15]. This analysis also uses the antineutrino-hydrogen scattering experimental data of Ref. [16], which is measured on a hydrocarbon target with kinematic separation of the events on hydrogen from the carbon background. Complementary constraints originating from LQCD are also explored in a sister paper [17], which will be compared to and combined with experimental sources in the present work.

Additional constraints on the slope of the form factor near zero momentum transfer could be obtained from additional pion electroproduction data [6] and muonic hydrogen [18]. The slope can be extracted from pion electroproduction data by comparing to a prediction obtained from expanding the amplitude for small Q^2 and M_π in heavy baryon chiral perturbation theory at one-loop order, such as in Ref. [19], where the slope shows up as a low energy constant in the effective theory. The pion electroproduction amplitudes are typically computed close to the pion production threshold, around $Q^2 \sim 0.1$ GeV^2 [20–22], and at this scale corrections can enter at the level of 10% [19]. For more details on the relationship between

invariant amplitudes and the differential cross sections, see for example Ref. [22]. The muonic hydrogen capture rate is also sensitive to the axial form factor at a momentum transfer fixed by kinematics, around a value of $Q^2 \sim 0.01\ \mathrm{GeV}^2$ [23–25]. Constraints on the axial radius from muon capture enter at about the 50% level [18], with an uncertainty budget dominated by statistics. Studies of constraints on the slope from these other sources are outside the scope of this work.

The sections in this paper are organized as follows. In Sec. II, details of the experimental datasets and fits employed in this work are discussed. Section III discusses the particulars of fitting data and evaluation of systematic uncertainties based on these fits. Section IV contains the final results from fitting including quantified uncertainties. Section V discusses the results of this work and their implications on experiments that involve neutrino scattering.

II. FIT DETAILS

This section focuses on the details associated with fitting data from neutrino quasielastic scattering off of both hydrogen and deuterium targets. The primary observable of interest is the flux-integrated neutrino-nucleon quasielastic scattering cross section. The differential cross section is used to fit the nucleon axial form factor, F_A, as a function of the spacelike 4-momentum transfer squared, Q^2.

After introducing the formalism in Sec. II A, the parametrization for F_A used in this work is outlined in Secs. II B and II C. Section II D gives an overview of the datasets and systematic corrections applied to those datasets that are relevant for this work. The remaining Secs. II E and II F deal with the specifics for making theory predictions of the flux-integrated differential cross section from the available information about the datasets.

A. Differential quasielastic scattering cross section

The neutrino-nucleon quasielastic cross section for an isosymmetric, unpolarized target is given as a function of Q^2 and neutrino energy E_ν by [26,27]

$$\frac{d\sigma_N}{dQ^2}(Q^2,E_\nu) = \frac{G_F^2 M_N^2 |V_{ud}|^2}{8\pi E_\nu^2}\left[A(Q^2) \pm \frac{(s-u)}{M_N^2}B(Q^2) + \frac{(s-u)^2}{M_N^4}C(Q^2)\right], \tag{2}$$

where the sign on the B term is taken to be positive (negative) for neutrino (antineutrino) scattering and the neutrino is assumed to be massless. In this expression, G_F is the Fermi constant, M_N is the average nucleon mass, V_{ud} is the Cabibbo–Kobayashi–Maskawa matrix element, and the kinematic expansion parameter is

$$s - u = 4M_N E_\nu - Q^2 - m_\ell^2, \tag{3}$$

which depends on the lepton mass m_ℓ. Neglecting second-class currents, the expressions A, B, and C are given in terms of form factors,

$$A = \frac{m_\ell^2 + Q^2}{M_N^2}\left[(1+\tau)F_A^2 + \tau(F_1+F_2)^2 - (F_1 - \tau F_2)^2 - \frac{m_\ell^2}{4M_N^2}\left((F_1+F_2)^2 + (F_A+2F_P)^2 - 4(1+\tau)F_P^2\right)\right], \tag{4}$$

$$B = 4\tau F_A(F_1+F_2), \tag{5}$$

$$C = \frac{1}{4}(F_A^2 + F_1^2 + \tau F_2^2). \tag{6}$$

These expressions use the dimensionless kinematic parameter $\tau = Q^2/4M_N^2$. In the limit of high E_ν, the kinematic prefactors on the A and B terms become small compared to that of C, and Eq. (2) becomes essentially independent of E_ν.

The four relevant form factors are the vector form factors F_1 and F_2, the induced pseudoscalar form factor F_P, and the axial form factor F_A, which all have functional dependence on Q^2. The vector form factors are taken from Refs. [28,29],[1] with the latter being used as the default choice. The vector form factors are assumed to be precisely known, and the impact of their uncertainty will be assessed in Sec. III D 2. By imposing the partially conserved axial current (PCAC) [31] and pion pole dominance (PPD) [32] constraints, the induced pseudoscalar current is related to the axial form factor with the expression

$$F_P = \frac{2M_N^2}{M_\pi^2 + Q^2}F_A. \tag{7}$$

The PCAC relation imposes a Ward identitylike relation between the divergence of the axial current and the pseudoscalar current, proportional to the sum of the quark masses rather than the difference. PPD then assumes that the new pseudoscalar form factor that appears is dominated by the pion pole through the Goldberger-Treiman relation, which imposes a constraint connecting the pseudoscalar form factor to the induced pseudoscalar and allows the pseudoscalar form factor to be removed.

The deviation of the induced pseudoscalar form factor from the combined PCAC and PPD relation is not expected to be significant. This assertion is supported by various studies with LQCD [33–38], which observe no statistically significant deviation from the PPD assumption in the

[1]This builds on a previous work by Ye *et al.* in Ref. [30] by optimizing the form factors for use at low Q^2.

continuum limit. Considering that all contributions of F_P to the differential cross section are also suppressed by a factor of $(m_\ell/M_N)^2$, the potential bias introduced assuming the PCAC and PPD constraints is expected to be small. It follows then that the leading contribution to the uncertainty of the quasielastic differential cross section is attributed to the nucleon axial form factor F_A.

B. z expansion parametrization

The z expansion is formulated as a conformal mapping to a small expansion parameter [39,40]. The transformation from 4-momentum transfer Q^2 to z is given as

$$z(Q^2; t_c, t_0) = \frac{\sqrt{t_c + Q^2} - \sqrt{t_c - t_0}}{\sqrt{t_c + Q^2} + \sqrt{t_c - t_0}}. \tag{8}$$

The parameter $t_c \leq 9M_\pi^2$ is bounded by the particle production threshold, which is limited by 3π production for the axial channel. The value $Q^2_{z=0}$ that satisfies $z(Q^2_{z=0}; t_c, t_0) = 0$ is determined by the selection of $Q^2_{z=0} = -t_0$. The parameter t_0 is chosen for convenience and can be adjusted to decrease the maximum value of $|z|$ over the entire range of Q^2 probed by neutrino scattering experiments. The value of z satisfies the inequality $|z| < 1$ within the kinematic range $Q^2 \in (-t_c, \infty)$, guaranteeing a power series with a small expansion parameter within a range of momentum transfers relevant for quasielastic scattering. For brevity, the dependence of z on Q^2, t_c, and t_0 will be omitted in subsequent equations.

Having formulated the transformation from Q^2 to z, the form factors are now expressed as a power series in the parameter z as

$$F_A(z) = \sum_{k=0}^{\infty} a_k z^k. \tag{9}$$

In theory the sum contains an infinite number of terms, but in practice the sum is truncated at a finite order $k_{\max}$. To regulate the large momentum transfer behavior of the form factor, a sequence of sum rules is enforced with the constraints

$$\begin{aligned} &\left(\frac{\partial}{\partial z}\right)^n F_A(z)|_{z=1} = 0, \qquad n \in \{0, \ldots, 3\} \\ \Rightarrow &\sum_{k=n}^{k_{\max}} k(k-1)\ldots(k-n+1)a_k = 0. \end{aligned} \tag{10}$$

These sum rules have minimal impact on the shape of the form factor within the range of data, but prevent the form factor from exhibiting unbounded behavior in the $Q^2 \to \infty$ limit. This is useful for extrapolating the form factor outside of the range of data, as is needed for many Monte Carlo generators, while still retaining reasonable functional behavior. One additional sum rule is added to fix the intercept of the form factor to the axial coupling value in the PDG[2] [41],

$$F_A(Q^2 = 0) = g_A \Rightarrow -g_A + \sum_{k=0}^{k_{\max}} a_k z_0^k = 0 \tag{11}$$

where $z_0 = z(Q^2 = 0)$. This constraint is taken to be exact since the uncertainty on g_A is below the precision of the axial form factor probed by experiments. With the full set of four derivative sum rules and axial coupling constraint, a fit to a z expansion with $k_{\max}$ coefficients will have $k_{\max} - 4$ free parameters. The formulas needed to implement the sum rules with full precision are explicitly given in Appendix.

C. z expansion regularization

The power series coefficients of the z expansion are constrained by unitarity to be bounded and decreasing with increasing order [39]. The relative size of the coefficients is therefore not expected to be too large. This was the motivation for introducing a χ^2 penalty term in Ref. [8] of the form

$$\chi^2_{\text{penalty}}(\lambda) = \lambda \sum_{k=1}^{k_{\max}} \left| \frac{a_k}{a_0 \sigma_k} \right|^2, \tag{12}$$

where the nominal λ was previously taken to be 1. The size of the nominal prior widths on the coefficient ratios was taken to be

$$\sigma_k = \min[5, 25/k] \tag{13}$$

reflecting a modest prior width for low-order coefficients and more restriction on higher order coefficients.

In this work, the same penalty term as in Eq. (12) is employed to regulate the relative size of coefficients and the choice of width σ_k is retained. However, the value of λ is selected by imposing an L-curve heuristic, taking the optimal value of λ for a particular fit to be the point of minimum radius of curvature (or $\lambda = 0$ in cases where no minimum is observed). The final choice of λ is selected by finding a compromise that accommodates several different fit choices (including $k_{\max}$, t_0, and included datasets) as described in Sec. II A.

[2]This work uses the convention $g_A > 0$, whereas PDG reports the axial coupling with a convention $g_A < 0$. Note that Ref. [8] also uses a convention with $g_A < 0$, which amounts to a sign flip of all of the z expansion coefficients.

TABLE I. The list of datasets considered in this work. The columns of the table indicate the references for the dataset, the label used for the dataset, the scattering interaction considered, the type of distribution reported in the reference, the implementation of the flux uncertainty, and the cuts applied to the dataset.

References	Dataset	Interaction	Dist. type	Data cuts	Flux unc.
[43–46]	ANL	$\nu_\mu + \mathrm{D}$	dN/dQ^2	$Q^2 \geq \{0.06, 0.20\}$ GeV^2	dN/dE
[47]	BNL	$\nu_\mu + \mathrm{D}$	dN/dQ^2	$Q^2 \geq \{0.06, 0.20\}$ GeV^2	dN/dE
[48]	FNAL	$\nu_\mu + \mathrm{D}$	dN/dQ^2	$Q^2 \geq \{0.06, 0.20\}$ GeV^2	dN/dE
[13–15]	BEBC	$\nu_\mu + \mathrm{D}$	$d\sigma/dQ^2$	—	Scaled
[16,49]	MINERvA	$\bar{\nu}_\mu + p$	$d\sigma/dQ^2$	$1.5 \leq p_\mu \leq 20$ GeV, $\theta_\mu \leq 20°$	Covariance

D. Datasets and corrections

1. Experimental datasets

There are five experimental datasets that were studied in this work. Three of these datasets (ANL, BNL, and FNAL) were previously considered in Ref. [8]. The relevant information about each dataset is listed in Table I and these data are provided as Supplemental Materials [42].

The first two columns of Table I indicate the references for that dataset and the label applied to those data. The third column contains the scattering interaction that was considered, either corresponding to scattering with hydrogen ($\bar{\nu}_\mu + p$, MINERvA only) or deuterium ($\nu_\mu + \mathrm{D}$). The fourth column contains the type of distribution reported for the dataset, either as an event distribution (dN/dQ^2) or as a differential cross section ($d\sigma/dQ^2$). The way that each of these event distributions is handled will be discussed throughout the rest of this section.

The fifth column is the cuts applied to the data. There are again three options, related to the kinematics: "Q^2" indicates that the low-Q^2 bins are removed to avoid systematics associated with low momentum transfer. Further attempts to handle the low-Q^2 behavior are explained in Secs. II D 4 and II D 5. Two cuts to the 4-momentum transfer were applied, taking 0.06 and 0.20 GeV^2 to match the historical choices in Ref. [8], and the consequences of these cuts discussed in more detail in Sec. III C. The MINERvA dataset applies two other cuts: "p_μ," a cut on the outgoing muon momentum, and "θ_μ," a cut on the angle of the outgoing muon momentum. The outgoing momentum for the MINERvA dataset was restricted to the range $1.5 \leq p_\mu \leq 20$ GeV/c and the outgoing angle to be $\theta_\mu \leq 20°$. The remaining sixth column is described in the next subsection.

2. Flux uncertainty

The last column of Table I is the method that was applied to capture the uncertainty due to the neutrino flux. There are three options listed. For the ANL, BNL, and FNAL datasets, labeled with "dN/dE," the flux uncertainty is applied to the bins of the neutrino energy event distribution. Each bin in the energy event distribution is allowed to float independently with a series of nuisance parameters η_i as

$$\left[\frac{dN}{dE_\nu}(\vec{\eta})\right]_i = \left[\frac{dN}{dE_\nu}\right]_i + \eta_i \left[\delta\frac{dN}{dE_\nu}\right]_i \tag{14}$$

where $\delta[dN/dE_\nu]_i$ is the statistical uncertainty on the event distribution in bin i. Each nuisance parameter η_i is priored with a Gaussian penalty of 0 ± 1.

In the case of the "scaled" flux uncertainty for BEBC, all bins in the $d\sigma/dQ^2$ distribution were allowed to float with a single normalization across all bins,

$$\mathcal{N}(\tilde{\eta}) = 1 + \tilde{\eta} d\mathcal{N}, \tag{15}$$

where $d\mathcal{N}$ is the relative flux uncertainty over all bins and $\tilde{\eta}$ is a nuisance parameter that is fit with the data. The nominal value of $d\mathcal{N}$ is chosen to be 0.10, and is compared to a value of 0.20 in Sec. III C 4. The nuisance parameter was also given a Gaussian penalty of 0 ± 1.

The "covariance" label for MINERvA indicates that the flux uncertainty was included in the covariance matrix for the $d\sigma/dQ^2$ distribution and so is not considered separately.

3. Normalizations

The ANL, BNL, and FNAL datasets, lack sufficient information to absolutely normalize the event distributions. The available distributions lack correlations between the event E_ν and Q^2. Without this information, there is a complicated interplay between the applied Q^2 cut, the differential cross section with its deuterium correction, and the flux uncertainty. When bins are removed from the differential cross section, the neutrino energy distribution must also be reduced to accurately implement the removal of low Q^2 events. The exact amount that each of the energy distribution bins should be reduced depends on the fraction of events that would fall into the Q^2 bins in question, which in turn depends on the assumed nucleon form factors and deuterium corrections for those Q^2 bins. It is therefore difficult to propagate the available flux uncertainties to the binned predictions.

To address this concern, the ANL, BNL, and FNAL datasets are fit with a normalization $\mathcal{N}$ that is allowed to float without an imposed prior. The flux uncertainty on the

BEBC dataset is captured through a floating normalization that is priored via Eq. (15). For the MINERvA dataset, the normalization is fixed to 1 as information about the flux uncertainty is embedded in the provided covariance.

4. Efficiency corrections

The deuterium bubble chamber experiments suffered from reduced efficiency—referred to as "acceptance" in Ref. [46]—when tracks were not prominent enough to measure accurately. This reduced efficiency primarily affected the low-Q^2 region and was accounted for with the efficiency correction

$$f(Q^2;\xi) = [\epsilon(Q^2) + \xi\delta\epsilon(Q^2)]^{-1} = \frac{1}{\epsilon(Q^2)}\left[1 + \xi\frac{\delta\epsilon(Q^2)}{\epsilon(Q^2)}\right]^{-1}. \quad (16)$$

The efficiency correction (ϵ) and its uncertainty ($\delta\epsilon$) used in this work was taken from Fig. 1 of Ref. [46]. The same form of the correction was applied to the ANL, BNL, and FNAL datasets with an independent ξ nuisance parameter for each dataset.

5. Deuterium corrections

For experiments with a deuterium target, a correction is needed to relate the free nucleon quasielastic cross section (σ_N) to the deuterium cross section (σ_{D}). This correction is typically assumed (as is the case in the present work) to be characterized by a ratio that depends only on Q^2,

$$\frac{d\sigma_{\mathrm{D}}}{dQ^2}(E_\nu, Q^2) \approx R(Q^2)\frac{d\sigma_N}{dQ^2}(E_\nu, Q^2). \quad (17)$$

The approach of marginalizing the deuterium correction into multiplicative corrections was discussed in Refs. [50,51].

The ratio $R(Q^2)$ should in general depend on the energy transfer ω, and consequently E_ν, as well. This can be seen by assuming an oversimplified approximation where the presence of a spectator proton inside of a deuterium nucleus forces the neutron to move with some Fermi momentum $\vec{p}$ relative to the two-nucleon center of mass system. Then the relationship between 4-momentum transfer squared and the energy transfer in quasielastic interactions takes the form

$$\omega = \frac{Q^2 + 2\vec{p}\cdot\vec{q}}{2E_N}. \quad (18)$$

In the special case of $\vec{p} = 0$, that yields an exact correspondence $\omega = Q^2/2M_N$. If a Lorentz boost were applied to cancel out the Fermi motion, then the effective E_ν as seen by the neutron at rest would be modified even though the Q^2 remains the same. Unless the distribution of neutron momenta within the deuterium nucleus conspired to cancel all ω dependence, both Q^2 and ω must therefore play separate roles in the deuterium correction. This kind of effect would be realized in nature by, for example, two-particle two-hole (2p2h) interactions in the deuterium nucleus. The short-range interactions characterizing the 2p2h are not included in the deuterium corrections of Singh [50] given in R but would modify the ω dependence at fixed Q^2, especially at low Q^2. Ideally the ratio could be promoted to depend on E_ν as well, choosing E_ν over ω because of the existing dependence on E_ν via the flux,

$$\frac{d\sigma_{\mathrm{D}}}{dQ^2}(E_\nu, Q^2) = R(E_\nu, Q^2)\frac{d\sigma_N}{dQ^2}(E_\nu, Q^2). \quad (19)$$

There are a number of concerns regarding the deuterium data, many of which relate to the low-Q^2 data. One immediate worry is that the deuterium effects are poorly understood, namely that the energies involved in neutrino scattering are sensitive to short-range interactions between nucleons inside the deuterium nucleus. Since no correction simultaneously exploring the ω and Q^2 dependence of the deuterium nucleus is readily available in the literature, this study is relegated to future works. The final quoted results from this work will not combine deuterium data with nucleon and hence will not be subject to the choice that is made for the form of R.

E. Handling event distributions

The ANL, BNL, and FNAL datasets report event distributions, which require different handling than flux-integrated differential cross sections. The relation used to compute the theory prediction for the event distribution in bin i is

$$\Delta Q_i^2\left[\frac{dN_{\mathrm{D}}}{dQ^2}\right]_i = \mathcal{N}\int_{\mathrm{bin}\,i} dQ^2 \int dE_\nu \times \left[f(Q^2)R(Q^2)\frac{d\Phi}{dE_\nu}(E_\nu)\frac{d\sigma_N}{dQ^2}(E_\nu, Q^2)\right]. \quad (20)$$

This relation depends on the normalization $\mathcal{N}$ (discussed in Sec. II D 3), the efficiency correction f [Eq. (16)], the deuterium correction R [Eq. (17)], and the flux Φ, which is determined from the event distribution over neutrino energy

$$\frac{d\Phi}{dE_\nu} = \frac{1}{\sigma(E_\nu)}\left[\frac{dN}{dE_\nu}\right]. \quad (21)$$

The cross section that appears in the denominator of Eq. (21) is obtained by integrating the differential cross section over Q^2,

$$\sigma(E_\nu) = \int dQ^2 \frac{d\sigma_N}{dQ^2}(E_\nu, Q^2). \quad (22)$$

This integration was carried out numerically with fixed free nucleon form factor parametrizations. The fits were allowed to run to completion with the fixed parametrizations, and then the parametrizations were updated to allow for variations in the form factors. After 4 iterations, the fit parameters had saturated such that further updates resulted in negligible shifts.

The neutrino flux for the FNAL dataset is at a high enough energy that the differential cross section becomes independent of E_ν, as discussed in the context of Eqs. (2)–(6). This means that the energy event distribution, $d\Phi/dE_\nu$, in Eq. (20) factorizes into a rescaling of the normalization factor $\mathcal{N}$. This simplification does not extend to the ANL and BNL datasets, which have event distributions that span much lower energy ranges. For these experiments, altering the neutrino flux amounts to uncontrolled changes to the form factor shape.

The integration over Q^2 and E_ν depends on both continuous functions as well as on binned datasets. The bin widths are sufficiently coarse that the continuous functions can change substantially over a single bin, which can lead to systematic effects due to binning. To suppress this effect, the data bins are subdivided to a finer resolution, and the binned data are kept constant over the entire coarse bin width. The functions are then computed at the bin center of each fine bin and summed over all bins.

To be explicit, the integration over the event distribution to obtain the flux is approximated as

$$\left[\int dE_\nu \frac{d\Phi}{dE_\nu}(E_\nu)\frac{d\sigma_N}{dQ^2}(E_\nu,Q^2)\right]_{\text{bin }j} \to \left[\frac{dN}{dE_\nu}\right]_j \left[\sum_{\text{bin }k\in\text{bin }j}\frac{\Delta E_{\nu,k}}{\sigma(E_{\nu,k})}\frac{d\sigma_N}{dQ^2}(E_{\nu,k},Q^2)\right], \quad (23)$$

where $\Delta E_{\nu,k}$ is the bin width of the fine bin k within coarse bin j and $E_{\nu,k}$ is the energy at the center of fine bin k. A similar procedure is applied for the integral over Q^2 bins,

$$\left[\int dQ^2 f(Q^2)R(Q^2)\frac{d\sigma_N}{dQ^2}(E_\nu,Q^2)\right]_{\text{bin }i} \to \sum_{\text{bin }k\in\text{bin }i}\Delta Q_k^2 f(Q_k^2)R(Q_k^2)\frac{d\sigma_N}{dQ^2}(E_\nu,Q_k^2). \quad (24)$$

In both cases, a resolution 10 times finer than the coarse binning was sufficiently fine that further sub-binning had a negligible effect on fit results.

F. Handling differential cross sections

The BEBC and MINERvA datasets both report flux-integrated differential cross sections that can be absolutely normalized. Both BEBC and MINERvA also span ranges of E_ν where the differential cross section is approximately energy independent. As a consequence, modifications to the flux are largely absorbed by any uncertainty associated with the absolute normalization of the data. For both of these experiments, the flux-integrated differential cross section $d\tilde{\sigma}_{(N,\mathrm{D})}/dQ^2$ for bin i with either a nucleon (N) or deuterium (D) target is

$$\Delta Q_i^2\left[\frac{d\tilde{\sigma}_{(N,\mathrm{D})}}{dQ^2}\right]_i = \frac{\mathcal{N}}{\tilde{\Phi}}\int_{\text{bin }i} dQ^2 R(Q^2)\int dE_\nu \times\left[\frac{d\Phi}{dE_\nu}(E_\nu)\frac{d\sigma_N}{dQ^2}(E_\nu,Q^2)\right]. \quad (25)$$

The denominator includes the flux integrated over energy,

$$\tilde{\Phi} = \int dE_\nu\left[\frac{d\Phi}{dE_\nu}(E_\nu)\right] = \sum_j \Delta E_{\nu,j}\left[\frac{d\Phi}{dE_\nu}\right]_j. \quad (26)$$

The efficiency correction discussed in Sec. II D 4 are not included in either the MINERvA or BEBC datasets.

Like with the event distributions, the integrals in Eq. (25) are discretized on a finer resolution to reduce binning systematics. The relevant integrals are

$$\left[\int dE_\nu \frac{d\Phi}{dE_\nu}(E_\nu)\frac{d\sigma_N}{dQ^2}(E_\nu,Q^2)\right]_{\text{bin }j} \to \left[\frac{d\Phi}{dE_\nu}\right]_j\left[\sum_{\text{bin }k\in\text{bin }j}\Delta E_{\nu,k}\frac{d\sigma_N}{dQ^2}(E_{\nu,k},Q^2)\right] \quad (27)$$

and again Eq. (24) but with $f(Q^2)=1$ fixed.

There are a few differences between BEBC and MINERvA worth noting. For the BEBC dataset, the normalization factor $\mathcal{N}$ is given in Eq. (15), which includes the flux uncertainty. The deuterium correction $R(Q^2)$ is the same as used in the other deuterium datasets, as discussed in Sec. II D 5. For the MINERvA dataset, the normalization is instead fixed to $\mathcal{N}=1$ and the deuterium correction taken to be $R(Q^2)=1$. Any uncertainty in the flux is included in the covariance matrix reported by the MINERvA collaboration. In addition, the antineutrino-nucleon differential cross section is used for $d\sigma_N/dQ^2$ rather than the neutrino-nucleon differential cross section used in BEBC.

III. FITTING

In this section, the results of fits are discussed. In particular, the compatibility of the input datasets is scrutinized to determine the most accurate depiction of the neutrino-nucleon quasielastic axial form factor and its uncertainty.

The default set of parameters used in this reference are listed in Table II.

TABLE II. A list of parameters needed to evaluate the differential cross sections. The first column gives the fit parameter, the second column lists the parameters used in Ref. [8], and the third column gives the parameters used in this work.

Parameter	Ref. [8]	This work
g_A	1.2723	1.2754 [41]
t_c	$9 \cdot (0.14\ \mathrm{GeV})^2$	$9 \cdot (0.134\ \mathrm{GeV})^2$
t_0	$-0.28\ \mathrm{GeV}^2$	$-0.50\ \mathrm{GeV}^2$
# sum rules	4	4
M_π	0.1395702 GeV	0.1395702 GeV
m_μ	0.1057 GeV	0.1056583755 GeV
μ_p	2.7928	2.7928
μ_n	−1.9130	−1.9130
M_N	0.9389 GeV	0.93891875434 GeV
$\cos\theta_C$	0.9743	0.9743
G_F	$1.166 \times 10^{-5}\ \mathrm{GeV}^{-2}$	$1.166 \times 10^{-5}\ \mathrm{GeV}^{-2}$
Vector FFs	BBBA05 [28]	Borah *et al.* [29]

A. L–curve studies and parametrization selection

One of the first tasks is to select a nominal parametrization to use for the form factor. This includes the selection of t_0 and $k_{\max}$ for use in the following fits comparing datasets. The sensitivity to these inputs will depend on how strongly prior constraints on parameters of the z expansion are enforced, and this strength is controlled by the parameter λ in Eq. (12).

In previous work [8], the penalty strength λ was assumed based on arguments from unitarity constraints. In this work, a data-driven L-curve approach [52,53] will be employed to select λ in order to avoid bias in the fit parameters. It is worth noting that either choice is an acceptable heuristic and ideally any results should not depend strongly on such a choice.

The L-curve approach compares the data contribution χ^2_{data} versus the penalty contribution $\chi^2_{\mathrm{penalty}}$ under variations of the penalty λ to find the point where the two competing χ^2 constraints are balanced. A penalty term that is too strong may introduce bias into the fit results, while a weak penalty with too many fit parameters could result in overfitting. When some parameters are constrained primarily by the penalty term, a healthy L-curve will exhibit an L-shaped bend and the "optimal" choice is taken at the point with a minimum radius of curvature. If few enough parameters are used, the $\chi^2_{\mathrm{penalty}}$ term may go to 0 as $\lambda \to 0$ without exhibiting a bend, indicating that no penalty term is required. Additional parameters are warranted as long as the corresponding change to the augmented χ^2,

$$\chi^2_{\mathrm{aug}} = \chi^2_{\mathrm{data}} + \chi^2_{\mathrm{penalty}} = \chi^2_{\mathrm{data}} + \lambda \sum_{k=1}^{k_{\max}} \left| \frac{a_k}{a_0 \sigma_k} \right|^2, \tag{28}$$

is commensurate with the decrease in the fit degrees of freedom to result in an improved fit quality: for each additional fit parameter, $\chi^2_{\mathrm{aug}}/\mathrm{DoF}$ should decrease, where DoF is the number of degrees of freedom. For this work, χ^2_{data} includes the squared residuals from the usual theory-data differences in the differential cross sections as well as statistical uncertainties for the flux [Eq. (14)] and priors for the efficiency corrections [Eq. (16)]. $\chi^2_{\mathrm{penalty}}$ includes only the regularization for the z expansion parameters and is defined in Eq. (12).

The fit L-curve for the MINERvA dataset in isolation is plotted in Fig. 1. This plot uses $t_0 = -0.5\ \mathrm{GeV}^2$ with various choices of λ and $k_{\max}$. The $k_{\max} = 5$ and $k_{\max} = 6$ curves exhibit no L-shape, indicating that the parametrizations are sufficiently well constrained by data that no regularization term is needed. The value of χ^2_{data} for $\lambda = 0$ only decreases by 0.2 when transitioning from $k_{\max} = 5$ to $k_{\max} = 6$. The $k_{\max} = 6$ parametrization (with 2 free parameters) produces only a marginally better χ^2_{data} than the $k_{\max} = 5$ parametrization (with 1 free parameter). The corresponding goodness-of-fit, $\chi^2_{\mathrm{aug}}/\mathrm{DoF}$, increases from $k_{\max} = 5$ to $k_{\max} = 6$, demonstrating a preference for $k_{\max} = 5$. The expected L-shape curve appears for $k_{\max} \geq 7$ with a point of minimum curvature around $\lambda \approx 0.2$. Additional fluctuation is seen in the left panel of Fig. 1, in particular for $k_{\max} = 8$ and $\lambda \approx 10^{-3}$, indicating that the

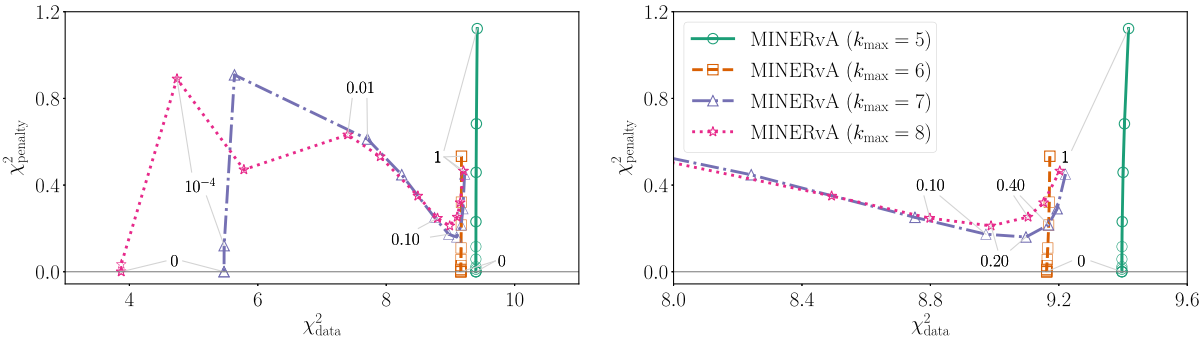


FIG. 1. L-curve obtained from fitting only the MINERvA dataset. The left plot shows the full range $\lambda \in [0, 1]$, and the right plot is zoomed in on the region with minimum radius of curvature. The numbers superimposed on the plot indicate the value of λ.

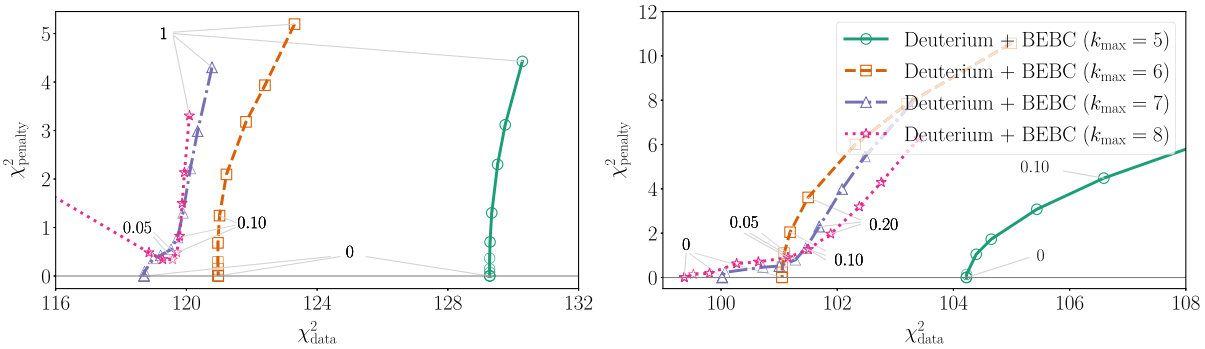


FIG. 2. L-curve obtained from fitting all of the deuterium datasets together. The left plot shows the $Q^2_{min} = 0.06$ GeV^2 cut, and the right plot the $Q^2_{min} = 0.20$ GeV^2 cut.

prior terms are not constraining enough to prevent the fit from falling into an unrealistic minimum.

Fig. 2 similarly shows L-curve plots for combined fits to all of the deuterium datasets. The two panels show the effect of different Q^2_{min} cuts on the L-curves for these datasets. Like the MINERvA dataset, the fits with $k_{max} = 5$ and $k_{max} = 6$ do not exhibit a distinctive L-shape, indicating that no penalty ($\lambda = 0$) is preferred. Unlike with the MINERvA dataset alone, there is a more substantial decrease in χ^2_{data} for $k_{max} = 6$ versus $k_{max} = 5$. These trends are exhibited for both Q^2 cuts.

In the left panel ($Q^2_{min} = 0.06$ GeV^2 cut), the $k_{max} = 7$ fit does exhibit a small L-shape around $\lambda \approx 0.02$ before $\chi^2_{penalty}$ again decreases with λ all the way to 0, indicating preference for a small regularization. $k_{max} = 8$ has a distinct L-shape bend around $\lambda \approx 0.1$ that denotes a clear preference for regularization. In the right panel ($Q^2_{min} = 0.20$ GeV^2 cut), both $k_{max} = 7$ and $k_{max} = 8$ behave as they do in the left panel, showing only slight preference for a nonzero λ. For the $Q^2_{min} = 0.06$ GeV^2 cut, the fits prefer regularized $k_{max} = 7$ with $\lambda = 0.05$, which has $\chi^2_{aug}/\text{DoF} \approx 1.09$, over unregularized $k_{max} = 6$ with $\chi^2_{aug}/\text{DoF} \approx 1.12$. This slight preference disappears for the $Q^2_{min} = 0.20$ GeV^2 cut, and again $k_{max} = 6$ with no regularization is the preferred fit strategy.

Although other parametrizations were tested, including variations of the choices for k_{max}, t_0, λ, and the included datasets, no appreciable departures from the general pictures described in Figs. 1 and 2 were seen. In isolation, the BEBC dataset L-curve behaves much like the MINERvA dataset does in Fig. 1. The L-curves for the deuterium event distributions without the BEBC dataset are very similar to those seen with all of the deuterium datasets together, shown in Fig. 2. Including all five datasets together again reproduces the same picture. The values of $t_0 \in \{0, -0.28, -0.50\}$ GeV^2 were tested to look for different preferred choices of values for k_{max} and λ, but no additional concerns arise for these choices.

Based on the considerations in this section, there are a few compromises that perform acceptably across all fit data. The two choices that will be considered henceforth, both with $t_0 = -0.50$ GeV^2, are

(1) $k_{max} = 6$ with no regularization ($\lambda = 0$), and
(2) $k_{max} = 7$ with $\lambda = 0.1$.

The former has the advantage of not being subject to dependence on the choice of regularization, while the latter gives a form factor parametrization with more freedom and presumably more conservative uncertainties. Both choices produce fits with similar fit quality in general, although the only instances where the $k_{max} = 7$ fits are preferred occur for the $Q^2_{min} = 0.06$ GeV^2 cut. No occurrences for $Q^2_{min} = 0.20$ GeV^2 were found where the change in χ^2_{data} was sufficient to offset the decrease in the degrees of freedom. The value $t_0 = -0.50$ GeV^2 is chosen to better capture some of the sensitivity to higher Q^2 from the MINERvA result. This choice of t_0 restricts the range $0 \le Q^2 \lesssim 2.55$ GeV^2 containing the majority of the events to satisfy $|z| \lesssim 0.34$, and has a maximal $z(Q^2 = 10\ \text{GeV}^2) \approx 0.60$.

B. χ^2 compatibility tests

The difference between data χ^2 values are used to compute p values in order to assess the compatibility between different fit assumptions. A 1-degree of freedom χ^2 test is constructed from the difference

$$\Delta\chi^2 = \chi^2_{A+B} - \chi^2_A - \chi^2_B, \tag{29}$$

where χ^2_A, χ^2_B, and χ^2_{A+B} are respectively the χ^2_{data} from fits to dataset A, dataset B, and both datasets A and B together. Two datasets that produce a p value ≥ 0.05 are considered to be compatible with each other and may be combined in a single fit without concern.

C. Minimum Q^2 cuts and regularization dependence

1. Event distribution datasets

In the ANL, BNL, and FNAL deuterium datasets, the low-Q^2 region requires the most care due to its sensitivity to

systematic effects. There are a few considerations to be conscious of:

(1) The tracks from the struck proton can be too short to reconstruct reliably at low Q^2, leading to poor efficiency and inaccurate characterization of the kinematics. Reference [46] estimates that the track reconstruction efficiency is about $89 \pm 7\%$ for events in the range $0.05 \leq Q^2 \leq 0.10$ GeV^2. The efficiency correction has been added to alleviate some of this effect. Although this problem will be worst at low Q^2, resolution is in principle a concern at all Q^2, and the papers describing the deuterium bubble chamber measurements give little insight into the treatment, save a comment in the FNAL paper stating that they only consider events where $\Delta p/p < 0.5$ [48].

(2) The spectator proton also cannot be reliably measured when it has small outgoing momentum. For momenta below 0.1 GeV/c, nearly all of the spectator protons are missed. Fits are employed to extract spectator momenta for these "two-prong" events assuming values centered at 0 and prior widths of around ± 50 MeV/c. The distributions are typically compared to a Hulthén wave function [54–56] to demonstrate the accuracy of the fit, but the majority of the events fall into the region where fits must be used for at least one of the proton tracks. The Hulthén wave function underpredicts the number of spectator protons in the high-momentum region where both protons can be directly observed. This high-momentum discrepancy is attributed to final state interactions in the literature.

(3) The corrections due to deuterium effects are assumed to be largest at low Q^2, due to Pauli exclusion principle for the low-momentum outgoing protons. The corresponding deuterium effect essentially turns off above $Q^2 \gtrsim 0.15$ GeV^2 in corrections applied to the data.

(4) Even with the corrections discussed here, the differential cross section data still exhibit a turnover at low-Q^2 that is too sharp to be well described by the fits.

To test the dependence on systematics due to the inclusion of low-Q^2 region, two different ranges of Q^2 are considered for the ANL, BNL, and FNAL deuterium datasets, as in Ref. [8]. The two Q^2_{min} cuts applied both with full regularization ($\lambda = 1$, left) and unregularized ($\lambda = 0$, right) are plotted in Fig. 3. The choice of $Q^2_{\text{min}} = 0.06$ GeV^2 was taken as the default in Ref. [8], which appears in Fig. 3 as the unfilled region bounded by two solid black lines. This is most similar to the teal shaded region, which only differs from the previously published results by choice of vector form factors and some fixed parameter inputs. This selection discards the first Q^2 bin, which is consistent with the practice employed in the original experimental publications. The other cut, $Q^2_{\text{min}} = 0.20$ GeV^2, was selected in Ref. [8] after considering several cuts and finding the minimum cut that would suppress sensitivity to k_{max}.

The left panel of Fig. 3 shows some moderate dependence on the minimum Q^2 cut. This was previously reported in Ref. [8], where the inability of the fit function to describe the low-Q^2 differential cross section data resulted in a significant degradation of the goodness-of-fit. When the constraint from the regularization is removed (right panel of Fig. 3), this inconsistency gets considerably worse. This is a consequence of an approximate degeneracy between the floating normalizations for the event distribution datasets (discussed in Sec. II D 3) and the axial form factor shape. Without the constraint of the z expansion parameter regularization, the a_k parameters are allowed to float arbitrarily far from 0 to deform the shape and better fit the curvature of the form factor. The change in the form factor scale from modifying the curvature is then absorbed into the floating normalizations.

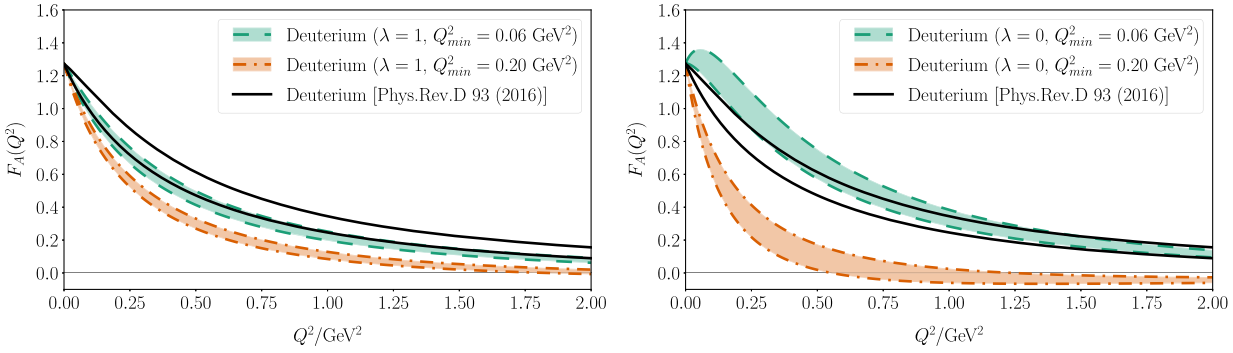


FIG. 3. Plots of the axial form factor as a function of the 4-momentum transfer Q^2. The left panel shows the regularized fits with $\lambda = 1$ and $k_{\text{max}} = 7$. The right panel shows the unregularized fits with $\lambda = 0$ and $k_{\text{max}} = 6$. The cut at $Q^2_{\text{min}} = 0.06$ GeV^2 is given by the teal shaded region bounded by a dashed line, and the cut at $Q^2_{\text{min}} = 0.20$ GeV^2 by the orange shaded region bounded by the dot-dashed line. The result from Ref. [8], which has $k_{\text{max}} = 8$ and $\lambda = 1$, is given by the unfilled region bounded by solid black lines.

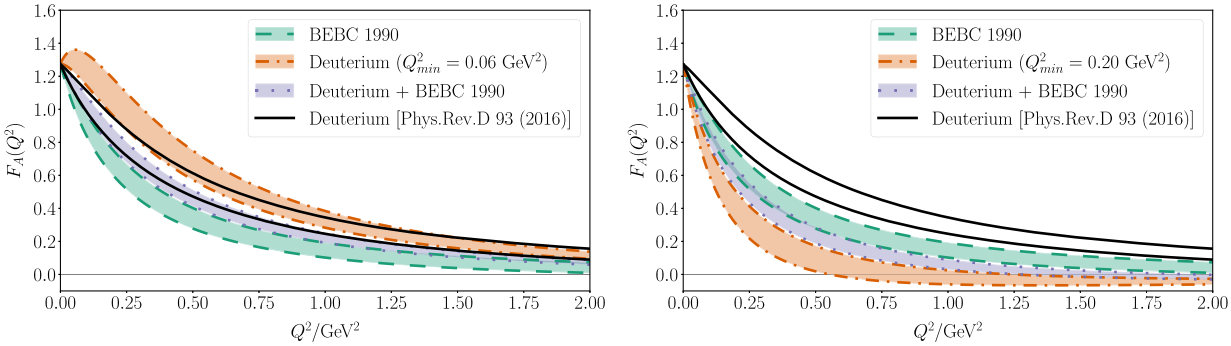


FIG. 4. The fit axial form factors both before and after the addition of the BEBC dataset to the other event distributions. In these fits, $k_{\max} = 6$ is chosen and the z expansion parameters are unregularized ($\lambda = 0$). The left (right) panel shows the form factors obtained when the 0.06 GeV^2 (0.20 GeV^2) cuts are applied to the event distribution datasets. The teal shaded region bounded by dashed lines indicates the fit only to the BEBC dataset (the same in both panels). The orange shaded region bounded by the dot-dashed line indicates the event-distribution datasets that were shown in the right panel of Fig. 3. The blue-violet shaded region bounded by the dotted line is the combined fit including both the event-distribution datasets and the BEBC dataset. The result from Ref. [8] is given by the unfilled region bounded by solid black lines.

2. Addition of BEBC dataset

A solution is needed for the degeneracy between the floating normalization and the axial form factor shape. A solution that does not appeal to introduction of a regularization would be preferable to one that does. Fortunately, the datasets with a flux-integrated differential cross section are absolutely normalized to within their flux uncertainty and are therefore not as sensitive to this degeneracy as the ANL, BNL, and FNAL datasets fit with a floating normalization. The BEBC dataset can therefore act as a source of constraint on the overall normalization of the event distribution datasets.

The effect of the addition of the BEBC dataset to a combined fit with the other event distribution datasets is shown in Fig. 4. The addition of the BEBC dataset has a nontrivial impact on the constraint of the form factor normalization, partially resolving the degeneracy. Without the BEBC dataset, the form factor shape at moderate Q^2 disagrees with the BEBC dataset by upward of $2-3\sigma$. After the addition of the BEBC dataset, the form factor is stable around the BEBC normalization within about 2σ. This situation is summarized in Fig. 5, where the BEBC dataset and combined fits are shown together.

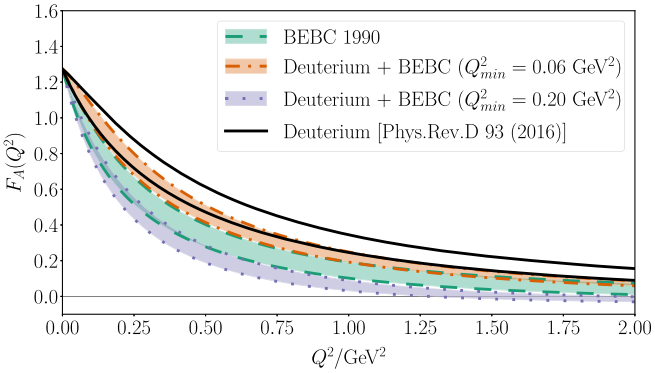


FIG. 5. The fit axial form factors for the BEBC dataset in isolation (teal shading, bounded by dashed line) and the combined fit with the event distribution datasets. The orange shaded region bounded by the dot-dashed line is the same joint-fit result shown in the left panel of Fig. 4. The blue-violet shaded region bounded by the dotted line is the same joint-fit result shown in the right panel of Fig. 4.

The results of the $\Delta\chi^2$ compatibility between the BEBC dataset and the other deuterium datasets are shown in Tables III and IV. In all cases, there is reasonable compatibility between the datasets. Better compatibility seen for $Q^2_{\min} = 0.20$ GeV^2, which has better goodness-of-fit than the $Q^2_{\min} = 0.06$ GeV^2 fit, and for the regularized $k_{\max} = 7$ fit, which has more fit parameters than the unregularized $k_{\max} = 6$ fit. The BEBC dataset is not subject to the $Q^2_{\min}$ cut and so the improvement in compatibility from changing the $Q^2_{\min}$ cut is entirely due to the removal of the poorly described low-Q^2 region in the event distribution datasets.

TABLE III. $\Delta\chi^2$ tests of compatibility for the deuterium event distributions and BEBC dataset. These values are for fits with $k_{\max} = 6$ and $\lambda = 0$. The two $Q^2_{\min}$ values are shown in the pairs of columns. Within the left column of each pair of columns, the χ^2_{data} for the two datasets in isolation are listed, then the χ^2_{data} for the combined fit, and finally the $\Delta\chi^2$ from Eq. (29). The right column of each pair shows the computed p value for the $\Delta\chi^2$ with 1 degree of freedom.

	$Q^2_{\min} = 0.06$ GeV^2		$Q^2_{\min} = 0.20$ GeV^2	
Fit	χ^2/DoF	$p_{\Delta\chi^2}$	χ^2/DoF	$p_{\Delta\chi^2}$
BEBC	6.1/6		6.1/6	
Deuterium	108.3/100		91.8/94	
Deuterium + BEBC	116.8/108		99.5/102	
$\Delta\chi^2$	2.5/1	0.11	1.6/1	0.20

TABLE IV. The same as Table III, but for $k_{\max} = 7$ and $\lambda = 0.1$.

	$Q^2_{\min} = 0.06$ GeV^2		$Q^2_{\min} = 0.20$ GeV^2	
Fit	χ^2/DoF	$p_{\Delta\chi^2}$	χ^2/DoF	$p_{\Delta\chi^2}$
BEBC	6.1/12		6.1/12	
Deuterium	108.3/106		93.2/100	
Deuterium + BEBC	116.2/114		100.2/108	
$\Delta\chi^2$	1.8/1	0.18	0.9/1	0.34

3. All deuterium versus MINERvA

The $\Delta\chi^2$ tests from Sec. III C 2 demonstrate that the complete set of four deuterium results are sufficiently compatible that they can be averaged together. However, the two different $Q^2_{\min}$ cuts still exhibit a $\sim 3\sigma$ shift due to the apparent degeneracy between normalization and form factor shape, seen in Fig. 5. Ideally, if the MINERvA hydrogen results are compatible with the complete set of deuterium results, these additional data would pin down the remnant degeneracy and remove this uncertainty, providing a precise axial form factor determination from all elementary target data sources. The compatibility between these datasets will be explored in more detail in this subsection.

A comparison of the MINERvA dataset to the rest of the deuterium datasets is shown in Fig. 6. Both sets of data have comparable constraints on the axial form factor uncertainty. However, a clear discrepancy between MINERvA and the deuterium can be seen at moderate and high Q^2 values for both $Q^2_{\min}$ cuts. MINERvA prefers a slower falloff than the deuterium datasets, larger by $> 2\sigma$ even for the lower $Q^2_{\min}$ cutoff. The combined fit including all datasets is dominated by the deuterium fits, exhibiting a slight pull toward the MINERvA but remaining mostly pinned to the deuterium result.

TABLE V. $\Delta\chi^2$ tests of compatibility comparing all deuterium datasets versus the MINERvA dataset. The format of this table is the same as for Table III. These values are for fits with $k_{\max} = 6$ and $\lambda = 0$.

	$Q^2_{\min} = 0.06$ GeV^2		$Q^2_{\min} = 0.20$ GeV^2	
Fit	χ^2/DoF	$p_{\Delta\chi^2}$	χ^2/DoF	$p_{\Delta\chi^2}$
All Deuterium	116.8/108		99.5/102	
MINERvA	9.2/11		9.2/11	
All	130.4/120		121.1/114	
$\Delta\chi^2$	4.4/1	0.04	12.4/1	4×10^{-4}

The $\Delta\chi^2$ compatibility tests comparing the MINERvA dataset to the deuterium datasets are shown in Tables V and VI. Although the p values are nearly acceptable for the $Q^2_{\min} = 0.06$ GeV^2 fits, and in fact the $k_{\max} = 7$ regularized fit in Table VI rounds up to $p_{\Delta\chi^2} = 0.05$, the agreement is artificial due to the additional poorly described fit data included in the lower Q^2 cut range. There are 6 data bins that are cut when increasing the cut from $Q^2_{\min} = 0.06$ GeV^2 to 0.20 GeV^2. The χ^2_{data} of the "all deuterium" fit in Table V decreases by 17.3 when those low-Q^2 data are cut, which is not commensurate with the decrease in the number of bins.

To further illustrate this incompatibility, consider the changes to χ^2 from inclusion of the MINERvA dataset. Comparing the "all deuterium" fits to the "all" fits in Table V, introduction of the MINERvA dataset (with 14 bins) increases χ^2_{data} by only 13.6 for $Q^2_{\min} = 0.06$ GeV^2, versus 21.6 for $Q^2_{\min} = 0.20$ GeV^2. The $\Delta\chi^2$ from each of these fit comparisons is almost entirely attributed to shifting the MINERvA data to accommodate the deuterium datasets: the contribution of the MINERvA dataset to χ^2_{data} of the "All" fit is 13.8 for $Q^2_{\min} = 0.06$ GeV^2 and 19.2 for

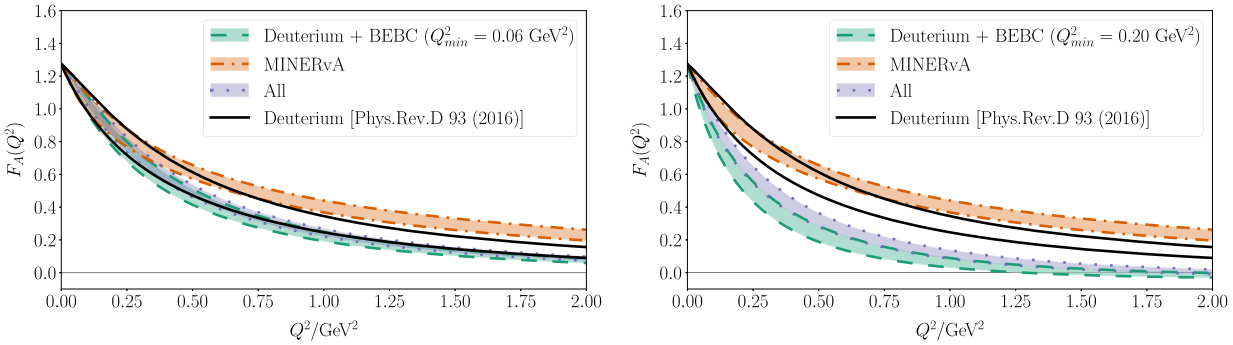


FIG. 6. Axial form factor results for fits comparing the complete set of deuterium data versus the MINERvA dataset. In these fits, $k_{\max} = 6$ is chosen and the z expansion parameters are unregularized ($\lambda = 0$). The left (right) panel shows the form factors obtained when the 0.06 GeV^2 (0.20 GeV^2) cuts are applied to the event distribution datasets. The teal shaded region bounded by dashed lines indicates the fit to the complete set of deuterium results, subject to the $Q^2_{\min}$ cut. The orange shaded region bounded by the dot-dashed line shows the fit to the MINERvA dataset in isolation (same in both panels). The blue-violet shaded region bounded by the dotted line is the combined fit to all datasets. The result from Ref. [8] is given by the unfilled region bounded by solid black lines.

TABLE VI. The same as Table V, except for fits with $k_{\max} = 7$ and $\lambda = 0.1$.

	$Q^2_{\min} = 0.06$ GeV^2		$Q^2_{\min} = 0.20$ GeV^2	
Fit	χ^2/DoF	$p_{\Delta\chi^2}$	χ^2/DoF	$p_{\Delta\chi^2}$
All Deuterium	116.2/114		100.2/108	
MINERvA	9.0/17		9.0/17	
All	129.2/126		121.3/120	
$\Delta\chi^2$	4.0/1	0.05	12.1/1	5×10^{-4}

$Q^2_{\min} = 0.20$ GeV^2 (a difference from the MINERvA fit χ^2_{data} in isolation by 4.6 and 10.0 respectively).

The $\Delta\chi^2$ difference for $Q^2_{\min} = 0.06$ GeV^2 is therefore less than for $Q^2_{\min} = 0.20$ GeV^2 only because poorly described low-Q^2 data tend to bias the axial form factor toward a shape that is not as far from the preferred shape of the MINERvA dataset. When these data are cut, the preferred "all deuterium" fit result shifts farther from the preferred MINERvA fit result. The p value degrades more significantly when the MINERvA data are added to the higher $Q^2_{\min}$ cut fit and the deuterium datasets are no longer considered to be compatible. Given other doubts cast by corrections due to the spectator nucleon in the deuterium nucleus, the unknown absolute normalization of the data, and potentially poorly characterized corrections to the low-Q^2 data, the deuterium datasets should be viewed with some skepticism.

This conclusion also comes in the historical context of predictions from LQCD results [11,34–38]. LQCD has consistently predicted a slower falloff of the axial form factor with respect to the other deuterium results, a conclusion that was presented concurrent with Monte Carlo tuning efforts with similar conclusions and before the public release of the MINERvA dataset. These statements from LQCD come after significant investment from multiple groups, including internal self-consistency checks as well as nontrivial cross-checks between different collaborations. Systematic effects from these calculations are understood and well-controlled. More detailed discussion about these comparisons is deferred to the sister paper, Ref. [17].

4. MINERvA-BEBC compatibility

Since agreement between MINERvA and the other deuterium datasets is contingent on inclusion of the poorly fit low Q^2 bins, the MINERvA dataset is considered to be inconsistent with the deuterium datasets. The lost correlations between Q^2 and E_ν of these historical deuterium event data and the absence of nuclear corrections in the MINERvA dataset lend credence to the MINERvA as the more accurate estimate of the form factor and its uncertainty. However, the BEBC dataset, which is presented as a differential cross section rather than an unnormalized event distribution and has a larger overall uncertainty when including the flux uncertainty, might still be sufficiently compatible with the MINERvA dataset to consider separately. This possibility is considered in this subsection.

TABLE VII. Table for $\Delta\chi^2$ tests of compatibility for BEBC and MINERvA datasets, in the same format as Table III. The two pairs of columns are for unregularized $k_{\max} = 6$ and regularized $k_{\max} = 7$ fits. These fits assume a 10% uncertainty on the flux normalization of the BEBC dataset.

	$k_{\max} = 6$ $\lambda = 0.0$		$k_{\max} = 7$, $\lambda = 0.1$	
Fit	χ^2/DoF	$p_{\Delta\chi^2}$	χ^2/DoF	$p_{\Delta\chi^2}$
BEBC	6.1/6		6.1/12	
MINERvA	9.2/11		9.0/17	
MINERvA + BEBC	21.2/18		20.8/24	
$\Delta\chi^2$	5.9/1	0.01	5.6/1	0.02

The $\Delta\chi^2$ tests for BEBC and MINERvA are given in Table VII. In these fits, a 10% flux uncertainty is assumed from the BEBC dataset. The same trend that was observed in Sec. III C 3 is seen again when the other deuterium datasets are removed. The combined fit to both BEBC and MINERvA also produces a modest increase in χ^2_{data} over the two datasets individually, with nearly all of the increase coming from the MINERvA contribution to the χ^2. For completeness, the $k_{\max} = 6$ unregularized combined fit contributes $\chi^2_{\text{data}} \sim 14.3$ from the MINERvA dataset, in contrast to only $\chi^2_{\text{data}} \sim 6.8$ from BEBC (compared to 9.2 and 6.1, respectively, from the second column of Table VII). Table VIII provides the same tests, but relaxes the BEBC normalization uncertainty to 20%. No substantial difference is seen for these fits, and the p values for $\Delta\chi^2$ still fall short of the acceptable range for compatibility.

This concludes the comparison of different datasets. Although the deuterium datasets are in agreement with each other, there is also a disagreement between the hydrogen dataset from MINERvA and the other deuterium datasets. This inconsistency implies that the form for $R(Q^2)$, or ratio of the deuterium to hydrogen cross section, is different from what is assumed. This shape dependence will be nontrivial to sort out because the differential cross section

TABLE VIII. The same as Table VII, but assuming a 20% uncertainty on the flux normalization of the BEBC dataset.

	$k_{\max} = 6$ $\lambda = 0.0$		$k_{\max} = 7$, $\lambda = 0.1$	
Fit	χ^2/DoF	$p_{\Delta\chi^2}$	χ^2/DoF	$p_{\Delta\chi^2}$
BEBC	6.0/6		6.1/12	
MINERvA	9.2/11		9.0/17	
MINERvA + BEBC	19.6/18		19.2/24	
$\Delta\chi^2$	4.5/1	0.03	4.1/1	0.04

bins with Q^2 are smeared out under the integration over the neutrino flux at low E_ν. More neutrino scattering measurements using hydrogen and deuterium targets will be necessary to sort out deuterium effects from flux effects. Until the time of these measurements, LQCD would be useful as an additional source of constraint on the nucleon axial form factor.

D. Systematics

In this section, systematics of the form factors are studied. Section III D 1 examines the effects of changing t_0, $k_{\max}$, and λ over the fits. Section III D 2 reports the changes and uncertainties given when replacing the vector form factor parametrization from Ref. [28] (referred to as the BBBA05 parametrization) with the z expansion parametrization from Ref. [29].

1. Parametrization choices

In principle, the parametrization choice should be insensitive to the choice of fit parameters t_0, $k_{\max}$, and λ. No statistically significant shifts are observed under the different fit choices made in this work.

Figure 7 shows the effects of choosing between the different truncations for the axial form factor power series. The value of λ is adjusted based on the preferred choices from the L-curve studies of Sec. III A. With the adjustment of λ, overfitting is avoided and the two results can be compared to each other directly. The two fits agree very well over the entire interesting Q^2 range with minimal deviation.

The selection of t_0 should be selected as a compromise to minimize the maximum value of $|z|$ in a range of Q^2 that is interesting for experiments. The choice $t_0 = -0.50$ GeV^2 used in this work more appropriately cover the range $0 < Q^2 < 6.0$ GeV^2 measured by the MINERvA experiment

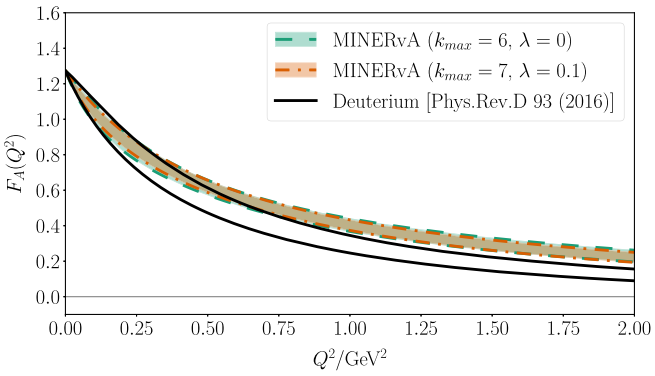


FIG. 7. The MINERvA dataset fit to different choices of $k_{\max}$ and λ. The $k_{\max} = 6$ fit is left unregularized ($\lambda = 0$), while $k_{\max} = 7$ requires a modest regularization parameter of $\lambda = 0.1$, as described in the text of Sec. III A. For reference, the form factor result from Ref. [8] is plotted as an unfilled region bounded by black lines.

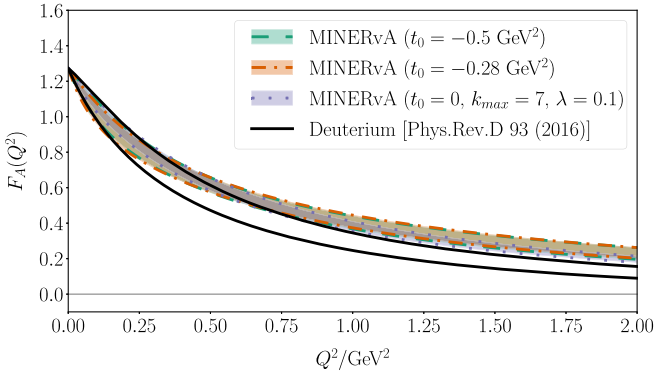


FIG. 8. The same as Fig. 8, but fit to different choices of t_0. The fits with $t_0 = -0.50$ GeV^2 and $t_0 = -0.28$ GeV^2 have $k_{\max} = 6$ and $\lambda = 0$. The fit to $t_0 = 0$ requires an additional change of $k_{\max}$ and λ.

than the choice $t_0 = -0.28$ GeV^2 used in Ref. [8]. The maximum value of $|z|$ (at $Q^2 = 6.0$ GeV^2) for this choice is around 0.51, versus $|z| \approx 0.58$ for $t_0 = -0.28$ GeV^2 and $|z| \approx 0.78$ for $t_0 = 0$. This choice is also optimized for evaluations within the range $0 < Q^2 < 2.0$ GeV^2, where $|z| \lesssim 0.33$, which is relevant for applications to long baseline neutrino oscillation experiments.

Figure 8 shows the shifts of using a different t_0 expansion point for the z expansion parametrizations. For $t_0 = -0.50$ GeV^2 and $t_0 = -0.28$ GeV^2, unregularized parametrizations with $k_{\max} = 6$ are appropriate to describe the form factor shape. When $t_0 = 0$, the range of $|z|$ is large enough such that a $k_{\max} = 6$ parametrization is no longer sufficient to describe the shape. The data are also not constraining enough to avoid overfitting without introduction of a light regularization term as well. However, when both of these considerations are taken into account, the final form factor shape is consistent with the other two choices of t_0.

2. Vector form factors

This subsection explores the effects of vector form factor parametrizations on the axial form factor shape and uncertainty. In Fig. 9, the result of replacing the BBBA05 parametrization for the vector form factors with the z expansion parametrization. As expected, no substantial difference is seen between the two choices. The axial form factor uncertainty is considerably larger than the difference between the parametrizations.

The uncertainty from the z expansion parametrization is propagated through the fits using principal component analysis with the covariance matrix reported in Ref. [29]. The mean values of the vector form factor parameters are shifted by the principal components extracted from the covariance matrix, then new fits are obtained. After the fit, the difference between the mean values for the axial form factor parameters of the nominal

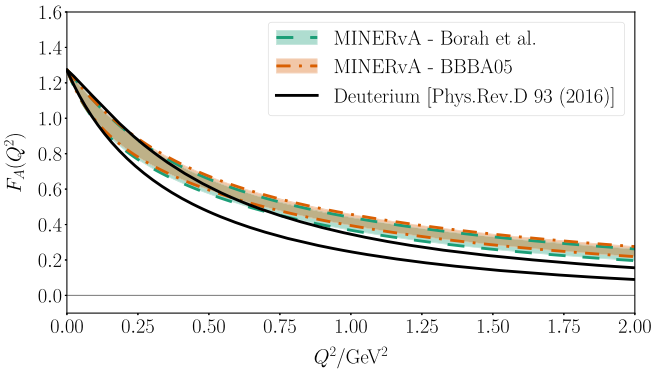


FIG. 9. The MINERvA dataset fit to both the BBBA05 vector form factor parametrization [28] (teal shading bordered by a solid line) and the z expansion vector form factor parametrization from Ref. [29] (orange shading bordered by a dashed line). For reference, the form factor result from Ref. [8], fit to the deuterium data, is plotted as an unfilled region bounded by black lines.

and shifted fits is taken as an additional uncertainty. The uncertainties from each of the eight principal components are then summed in quadrature.

IV. RESULTS

Various fit results are collected in this section. The central values with their uncertainties are reported along with the means for the full set of coefficients, including those constrained by sum rules, and the covariances of the fit parameters. The values listed here combined with the parameters in Table II are sufficient to reproduce the form factor curves shown in plots in this work. In addition, the axial radius squared is provided for comparison with experiments that are sensitive to low-Q^2 behavior of the form factor. The squared radius is related to the slope at $Q^2 = 0$ through the relation

$$r_A^2 = -\frac{6}{g_A}\frac{dF_A}{dQ^2}\bigg|_{Q^2=0}. \tag{30}$$

The fits with $k_{\max} = 6$ and $\lambda = 0$ are the recommended optimal choice of parameters. This is motivated by two observations:

(1) the L-curve study in Sec. III A for fits to the MINERvA dataset show that moving from an unregularized $k_{\max} = 5$ fit to an unregularized $k_{\max} = 6$ fit decreases χ^2_{aug} by only about 0.2, which when considered in isolation is insufficient to justify the increase $k_{\max} = 6$; and

(2) although the MINERvA fits prefer $k_{\max} = 5$, the p value is not significantly diminished at $k_{\max} = 6$ and so comparisons with LQCD, which prefer $k_{\max} = 6$, can be performed without adversely impacting the fit quality.

For evaluating systematics due to finite truncation of the z expansion parametrizations, the values for $k_{\max} = 7$ and $\lambda = 0.1$ fits (or $\lambda = 0$ for LQCD alone) are also reported.

In all cases considered, the value of the coefficient a_1 is consistent when moving from a $k_{\max} = 6$ to $k_{\max} = 7$ fit. The value of a_2 and r_A^2 can change by $\gtrsim 2\sigma$, suggesting that higher-order form factor shape effects are still not fully captured by truncation to $k_{\max} = 6$. The degraded p values for $k_{\max} = 7$ suggest that the data are not sufficiently constraining enough to justify the additional fit parameter and that the slight tensions might be the result of overfitting rather than the true data preference.

A. MINERvA hydrogen fit result

The final results from fits to the MINERvA data are listed in this subsection. The $k_{\max} = 6, \lambda = 0$ fit yields the z expansion parameters

$$(a_1, a_2) = (-1.65(24), 0.94(30)) \tag{31}$$

with the covariance matrix

$$\begin{pmatrix} 0.05554150 & -0.03262482 \\ -0.03262482 & 0.09151761 \end{pmatrix}. \tag{32}$$

With the sum rule constraints applied, the central values of the full set of coefficients are

$$\begin{aligned}(a_0, \ldots, a_6) \\ = \; & (0.61490770, \; -1.64778080, \; 0.94181417, \\ & 0.41239729, \; 0.36611559, \; -1.18722194, \\ & 0.49976799).\end{aligned} \tag{33}$$

The axial radius squared obtained from this parametrization is

$$r_A^2 = 0.575(222)\ \text{fm}^2. \tag{34}$$

This choice has a well-defined p value ≈ 0.69 from $\chi^2 \approx 9.16$ and 12 degrees of freedom.

The $k_{\max} = 7$ fit with the regularization parameter $\lambda = 0.1$ is also listed as a comparison point. The fit central values are

$$(a_1, a_2, a_3) = (-1.69(17), 0.81(34), 0.9(1.2)) \tag{35}$$

with the covariance matrix

$$\begin{pmatrix} 0.02771279 & -0.00093839 & -0.19136214 \\ -0.00093839 & 0.11854816 & -0.12082981 \\ -0.19136214 & -0.12082981 & 1.45823056 \end{pmatrix}. \tag{36}$$

With the sum rule constraints applied, the central values of the full set of coefficients are

$$\begin{aligned}&(a_0,\ldots,a_7)\\&\quad(0.62174048,\ -1.69373431,\ 0.80639393,\\&=\ 0.87442257,\ 0.55213983,\ -2.61742963,\\&\quad 1.85900234,\ -0.40253521).\end{aligned}\tag{37}$$

The axial radius squared obtained from this parametrization is

$$r_A^2 = 0.565(149)\ \text{fm}^2.\tag{38}$$

Treating the priors as additional data, the fit give a $p$value ≈ 0.96 from an augmented $\chi^2 \approx 9.14$ and 18 degrees of freedom. Ignoring the priors yields $p$value ≈ 0.62 from data $\chi^2 \approx 8.97$ and 11 degrees of freedom.

B. LQCD fit result

For comparison with the results in this work, the result of the sister paper [17] is reproduced here. The needed fit parameters match those listed in Table II. The $k_{\max} = 6$, $\lambda = 0$ fit is

$$(a_1, a_2) = (-1.701(42), 0.263(90))\tag{39}$$

with the covariance matrix

$$\begin{pmatrix} 0.00175929 & -0.00294651 \\ -0.00294651 & 0.00807158 \end{pmatrix}.\tag{40}$$

With the sum rule constraints applied, the full set of coefficients are

$$\begin{aligned}&(a_0,\ldots,a_6)\\&\quad(0.72115656,\ -1.70104640,\ 0.26324902,\\&=\ 1.53433681,\ 0.01061114,\ -1.49893610,\\&\quad 0.67062898).\end{aligned}\tag{41}$$

The axial radius squared obtained from this parametrization is

$$r_A^2 = 0.369(30)\ \text{fm}^2.\tag{42}$$

The unknown correlations between LQCD results prevent the assignment of a definitive p value. Instead, covariance derating [57] is used to estimate a 99% confidence interval upper bound on the goodness-of-fit. This limits $p$value $\lesssim 0.65$. Assuming the unknown correlations are identically 0, the p value can be computed directly as $p \approx 0.52$ from $\chi^2 \approx 7.14$ and 8 degrees of freedom.

The $k_{\max} = 7$, $\lambda = 0$ fit is

$$(a_1, a_2, a_3) = (-1.658(95), 0.431(347), 1.06(97))\tag{43}$$

with the covariance matrix

$$\begin{pmatrix} 0.00910412 & 0.02592048 & -0.08986544 \\ 0.02592048 & 0.12033231 & -0.30490195 \\ -0.08986544 & -0.30490195 & 0.93874891 \end{pmatrix}.\tag{44}$$

With the sum rule constraints applied, the full set of coefficients are

$$\begin{aligned}&(a_0,\ldots,a_7)\\&\quad(0.72240694,\ -1.65806627,\ 0.43099261,\\&=\ 1.06243035,\ -0.68256510,\ 1.06363538,\\&\quad -1.59271086,\ 0.65387696).\end{aligned}\tag{45}$$

The axial radius squared obtained from this parametrization is

$$r_A^2 = 0.341(62)\ \text{fm}^2.\tag{46}$$

In this case, derating the goodness-of-fit limits $p \lesssim 0.55$ at 99% confidence. Assuming the unknown correlations are all identically 0, $p \approx 0.43$ from $\chi^2 \approx 6.99$ and 7 degrees of freedom.

C. Previous deuterium fit result

In the interest of concrete comparisons, the deuterium results from Ref. [8] with $t_0 = -0.28\ \text{GeV}^2$ are converted to a z expansion parametrization with $t_0 = -0.50\ \text{GeV}^2$. This is possible because the z expansion power series coefficients are exactly proportional to the derivatives with respect to z at $Q^2 = -t_0$ (or $z = 0$). In other words, a z expansion parametrization satisfies the proportionality

$$a_k = \frac{1}{k!}\frac{d^k F_A(z)}{dz^k}\bigg|_{z=0}.\tag{47}$$

Therefore, a translated z expansion parametrization approximating another parametrization can be obtained by examining the central value and derivatives of another form factor parametrization at $Q^2 = -t_0$ using the new z expansion's definition of t_0. For more details, the reader is referred to Ref. [17].

Using the above prescription for translation, the z expansion from Ref. [8] with $k_{\max} = 8$ translated to a parametrization with the values listed in Table II and $k_{\max} = 6$ gives the coefficients

$$(a_1, a_2) = (-2.08(21), 1.90(37))\tag{48}$$

with the covariance matrix

$$\begin{pmatrix} 0.04304942 & 0.02482393 \\ 0.02482393 & 0.13790576 \end{pmatrix}.\tag{49}$$

With the sum rule constraints applied, the central values of the full set of coefficients are

$$
\begin{aligned}
&(a_0, \ldots, a_6) \\
&\quad (0.54264533, \quad -2.08493637, \quad 1.89831616, \\
&= \quad 2.40319245, \quad -5.88979056, \quad 4.14554900, \\
&\quad -1.01497601).
\end{aligned} \tag{50}
$$

This reproduces the form factor central value shape and magnitude with no more than 2% fractional deviation over the entire range 0–2 GeV^2. The axial radius squared obtained from this parametrization is

$$r_A^2 = 0.334(254)\ \text{fm}^2, \tag{51}$$

which is in agreement with the published value 0.46(22) fm^2.

Using the above prescription for translation, the z expansion from Ref. [8] with $k_{\max} = 8$ translated to a parametrization with the values listed in Table II and $k_{\max} = 7$ gives the coefficients

$$(a_1, a_2, a_3) = (-2.08(21), 1.53(48), 2.8(1.8)) \tag{52}$$

with the covariance matrix

$$\begin{pmatrix} 0.04304942 & 0.06034134 & -0.36481368 \\ 0.06034134 & 0.23520236 & -0.67627605 \\ -0.36481368 & -0.67627605 & 3.27220947 \end{pmatrix}. \tag{53}$$

With the sum rule constraints applied, the central values of the full set of coefficients are

$$
\begin{aligned}
&(a_0, \ldots, a_7) \\
&\quad (0.54264533, \quad -2.08493637, \quad 1.53196776, \\
&= \quad 2.78626545, \quad -3.75859858, \quad -0.88298095, \\
&\quad 2.94795795, \quad -1.08232059).
\end{aligned} \tag{54}
$$

This reproduces the form factor shape and magnitude with no more than 3% fractional deviation over the range 0–1 GeV^2 and no more than 10% over the range 0–2 GeV^2. The axial radius squared obtained from this parametrization is

$$r_A^2 = 0.434(215)\ \text{fm}^2, \tag{55}$$

which is in good agreement with the published value 0.46(22) fm^2.

D. Combined hydrogen-LQCD fit result

In this subsection, the MINERvA hydrogen data are fit simultaneous with the LQCD results from Ref. [17]. These results are used to create a $\Delta\chi^2$ comparison with which to assess the compatibility between the hydrogen and LQCD.

The result for a simultaneous fit to the LQCD results and the MINERvA dataset with $k_{\max} = 6$ and $\lambda = 0$ yields

$$(a_1, a_2) = (-1.717(41), 0.317(86)) \tag{56}$$

with the covariance matrix

$$\begin{pmatrix} 0.00165493 & -0.00268883 \\ -0.00268883 & 0.00737483 \end{pmatrix}. \tag{57}$$

With the sum rule constraints applied, the full set of coefficients are

$$
\begin{aligned}
&(a_0, \ldots, a_6) \\
&\quad (0.71592650, \quad -1.71743430, \quad 0.31652883, \\
&= \quad 1.58969769, \quad -0.23282053, \quad -1.27795482, \\
&\quad 0.60605663).
\end{aligned} \tag{58}
$$

The axial radius squared obtained from this parametrization is

$$r_A^2 = 0.364(30)\ \text{fm}^2. \tag{59}$$

The derated goodness-of-fit yields $p \lesssim 0.68$. With the unknown correlations set to 0, the goodness-of-fit is $p \approx 0.62$ from data $\chi^2 \approx 19.45$ and 22 degrees of freedom.

Assuming $k_{\max} = 7$ and $\lambda = 0$, the result is

$$(a_1, a_2, a_3) = (-1.776(76), 0.05(29), 2.27(77)) \tag{60}$$

with the covariance matrix

$$\begin{pmatrix} 0.00576457 & 0.01550765 & -0.05596858 \\ 0.01550765 & 0.08687614 & -0.19816291 \\ -0.05596858 & -0.19816291 & 0.59358115 \end{pmatrix}. \tag{61}$$

With the sum rule constraints applied, the full set of coefficients are

$$
\begin{aligned}
&(a_0, \ldots, a_7) \\
&\quad (0.71531031, \quad -1.77604402, \quad 0.04912094, \\
&= \quad 2.27409531, \quad 0.89742871, \quad -5.20892371, \\
&\quad 4.03266727, \quad -0.98365481).
\end{aligned} \tag{62}
$$

The axial radius squared obtained from this parametrization is

$$r_A^2 = 0.408(55)\ \text{fm}^2. \tag{63}$$

With this fit, the derated goodness-of-fit is $p\text{value} \lesssim 0.65$ at 99% confidence. Without correlations, the goodness-of-fit is $p \approx 0.59$ from augmented $\chi^2 \approx 18.91$ and 21 degrees of freedom.

The $\Delta\chi^2$ compatibility comparison between the MINERvA and LQCD datasets for the $k_{\max} = 6$ fits are shown in Table IX. Both the tests when ignoring the unknown correlations of the LQCD (labeled as "ignore

TABLE IX. The $\Delta\chi^2$ fit compatibility test between the MINERvA and LQCD fits. Due to the presence of unknown correlations between the LQCD results, the compatibility test is split into two computations: the first ("ignore unknown") assumes that all of the unknown correlations are exactly 0, and the second ("derate") uses the covariance derating [57] technique to extract a 99% confidence interval upper bound on the p value from allowed covariance variations. For each fit, the χ^2 and DoF are reported. The $\Delta\chi^2$ from Eq. (29) is reported in the last line along with a p value for the 1 DoF $\Delta\chi^2$ check.

	Ignore unknown		Derate	
Fit	χ^2/DoF	$p_{\Delta\chi^2}$	χ^2/DoF	$p_{\Delta\chi^2}$
LQCD	7.1/8		6.0/8	
MINERvA	9.2/16		9.2/16	
MINERvA + LQCD	19.5/22		18.5/22	
$\Delta\chi^2$	3.2/1	0.08	3.4/1	0.07

unknown") and using the covariance derating ("derating") are listed. Although there is some apparent tension in the Q^2 shape of the two fits, the tension only has a mild effect on the combined fit χ^2. The resulting combined fit is largely dominated by the LQCD fit such that the increase in χ^2 for the combined fit is almost entirely due to the MINERvA residuals increasing. The p values for both choices of correlation treatment are above the 5% threshold to consider them compatible.

E. Deuterium fit results

This subsection lists the results for combined deuterium fits including the results of ANL, BNL, FNAL, and BEBC datasets together. All fits in this section assume that the normalization on the BEBC flux is 10%. The results will be used to produce error envelopes describing the full range of potential form factor shapes allowed by the deuterium data. These results are listed for completeness but caution is advised when using these results because of the issues discussed throughout this work.

The fit results for the $k_{\max} = 6$ fit with a data cut at $Q^2_{\min} = 0.06$ GeV^2 are

$$(a_1, a_2) = (-2.10(16), 2.46(20)) \tag{64}$$

with a covariance matrix

$$\begin{pmatrix} 0.02429039 & 0.02129680 \\ 0.02129680 & 0.03924659 \end{pmatrix}. \tag{65}$$

The full precision coefficients after computing sum rules are

$$\begin{aligned}(a_0, \ldots, a_6) \\ = (&0.46232604, -2.09518344, 2.46409998, \\ &1.84891368, -6.31439714, 4.92761426, \\ &-1.29337338).\end{aligned} \tag{66}$$

The computed axial radius squared is

$$r_A^2 = 0.449(194)\ \text{fm}^2. \tag{67}$$

This fit yields $\chi^2_{\text{aug}} \approx 121.0$ and $\chi^2_{\text{data}} \approx 116.8$ with 108 degrees of freedom.

The fit results for the $k_{\max} = 6$ fit with a data cut at $Q^2_{\min} = 0.20$ GeV^2 are

$$(a_1, a_2) = (-1.73(15), 3.64(20)) \tag{68}$$

with a covariance matrix

$$\begin{pmatrix} 0.02362940 & 0.02199389 \\ 0.02199389 & 0.04075856 \end{pmatrix}. \tag{69}$$

The full precision coefficients after computing sum rules are

$$\begin{aligned}(a_0, \ldots, a_6) \\ = (&0.23685629, -1.72881714, 3.63918001, \\ &-2.00567449, -2.08272958, 2.84871053, \\ &-0.90752562).\end{aligned} \tag{70}$$

The computed axial radius squared is

$$r_A^2 = 1.091(193)\ \text{fm}^2. \tag{71}$$

This fit yields $\chi^2_{\text{aug}} \approx 101.1$ and $\chi^2_{\text{data}} \approx 99.5$ with 102 degrees of freedom.

The fit results for the $k_{\max} = 7$ fit with a data cut at $Q^2_{\min} = 0.06$ GeV^2 are

$$(a_1, a_2, a_3) = (-2.01(13), 2.08(31), 1.6(1.1)) \tag{72}$$

with a covariance matrix

$$\begin{pmatrix} 0.01810872 & 0.01599862 & -0.14396435 \\ 0.01599862 & 0.09367352 & -0.21192733 \\ -0.14396435 & -0.21192733 & 1.23483538 \end{pmatrix}. \tag{73}$$

The full precision coefficients after computing sum rules are

$$\begin{aligned}(a_0, \ldots, a_6) \\ = (&0.44565733, -2.00572162, 2.08155251, \\ &1.62372606, -2.79400350, -1.44885058, \\ &3.29177330, -1.19413349).\end{aligned} \tag{74}$$

The computed axial radius squared is

$$r_A^2 = 0.657(176)\ \text{fm}^2. \tag{75}$$

This fit yields $\chi^2_{\text{aug}} \approx 120.5$ and $\chi^2_{\text{data}} \approx 116.2$ with 114 degrees of freedom.

The fit results for the $k_{\text{max}} = 7$ fit with a data cut at $Q^2_{\text{min}} = 0.20\ \text{GeV}^2$ are

$$(a_1, a_2, a_3) = (-2.01(13), 2.08(31), 1.6(1.1)) \tag{76}$$

with a covariance matrix

$$\begin{pmatrix} 0.01810872 & 0.01599862 & -0.14396435 \\ 0.01599862 & 0.09367352 & -0.21192733 \\ -0.14396435 & -0.21192733 & 1.23483538 \end{pmatrix}. \tag{77}$$

The full precision coefficients after computing sum rules are

$$\begin{aligned}(a_0, \ldots, a_6) \\ = (&0.44565733, \ -2.00572162, \ 2.08155251, \\ &1.62372606, \ -2.79400350, \ -1.44885058, \\ &3.29177330, \ -1.19413349).\end{aligned} \tag{78}$$

The computed axial radius squared is

$$r_A^2 = 0.657(176)\ \text{fm}^2. \tag{79}$$

This fit yields $\chi^2_{\text{aug}} \approx 102.8$ and $\chi^2_{\text{data}} \approx 100.2$ with 108 degrees of freedom.

F. Summary of fits

The set of results described in this work is shown in Fig. 10. As discussed in the manuscript, the deuterium suffers from a strong dependence on the prior assumptions. As an attempt to capture the full spread of this dependence, the extreme bounds of the two Q^2_{min} cuts, with the lower bound taken from Eqs. (68) and (69) and the upper bound from Eqs. (64) and (65), are used to produce an uncertainty envelope for the datasets. This spread would be even worse without the inclusion of the BEBC dataset. Even with the inflated uncertainty, the extreme bounds fall significantly below the other results at larger Q^2 and more than 1σ for even the results of Ref. [8]. Above $Q^2 \approx 1.25\ \text{GeV}^2$, the sign of the form factor is not constrained at more than 1σ.

Although the $\Delta\chi^2$ test described in Table IX passes a $p$value ≥ 0.05 test, the MINERvA and LQCD fits appear to have slightly different values across Q^2 in Fig. 10, outside of the uncertainty of either fit. As seen in the comparison of Eq. (31) to Eq. (39), this is primarily due to the difference in the second-order parameter a_2, which differs by approximately two standard deviations in the two fits. However, this tension is only at the modest 2σ level in a_2. With this interpretation, it is easy to understand the correlation in the difference across all values of Q^2.

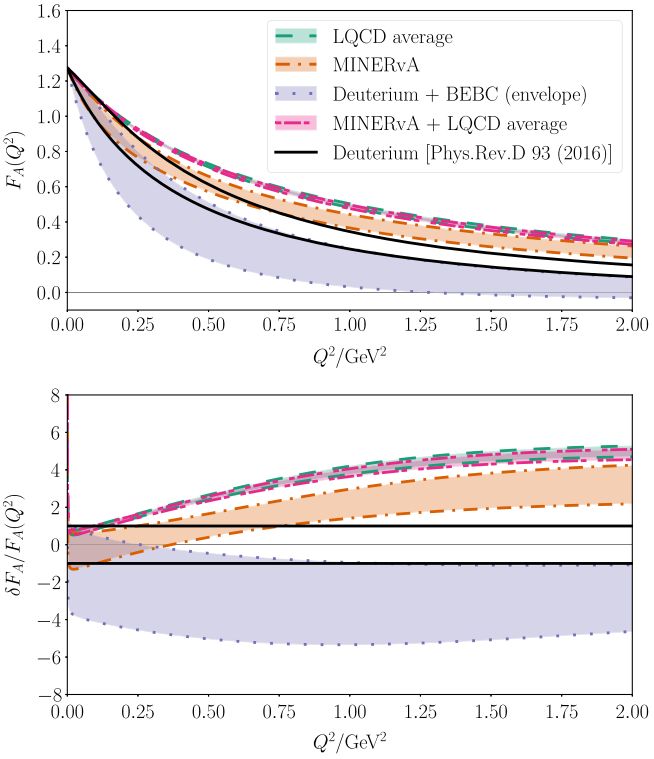


FIG. 10. The top panel shows the final choices for the axial form factor parametrizations after the fits discussed in this work. The bottom panel shows those same parametrizations normalized to the deuterium result of Ref. [8]. The MINERvA and LQCD average fits are obtained from Eqs. (31) and (39), respectively. The bounds for the curve labeled "Deuterium+BEBC (envelope)" are obtained from the lower bound of the "Deuterium+BEBC ($Q^2_{\text{min}} = 0.20\ \text{GeV}^2$)" and the upper bound of the "Deuterium +BEBC ($Q^2_{\text{min}} = 0.06\ \text{GeV}^2$)" curves in Fig. 5. The MINERvA + LQCD average fit is taken from Eq. (56).

Another test of compatibility is the p value obtained from the MINERvA residuals for both the MINERvA-only and joint fits. For the joint fit, we find $\chi^2_{\text{MINERvA}} \approx 12.10$ for 12 degrees of freedom, yielding $p \approx 0.44$. This is to be compared with MINERvA values in Table IX, with $\chi^2_{\text{MINERvA}} \approx 12.10$ for 12 degrees of freedom and $p \approx 0.69$. Because of the greater precision of the LQCD constraints relative to those of MINERvA, the joint fit does not significantly change the MINERvA residuals, even if the uncertainty band appears to be far from the MINERvA result."

There is another zero parameter prediction of the axial form factor in the literature based on an axial vector meson dominance model [58]. It provides a prediction which is consistent with the LQCD and MINERvA form factors, within uncertainties of the model and these fit results, albeit with a visibly larger form factor for $Q^2 > 0.2\ \text{GeV}^2$ as shown in Fig. 11.

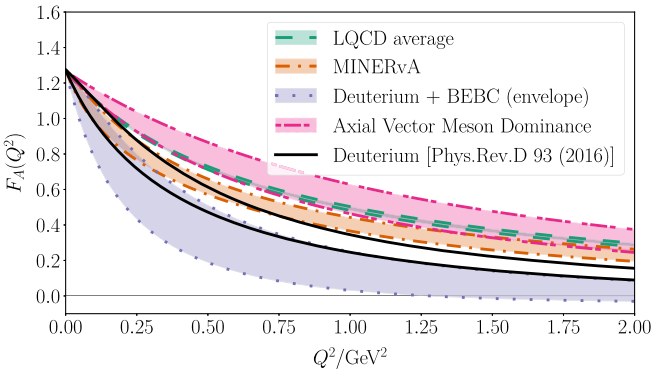


FIG. 11. The same as the top panel of Fig. 10, but with the addition of the axial vector meson dominance model (pink shaded region with a triple-dash boundary). The form factor curve from the combined fit, Eq. (56), only has minor deviations from the LQCD fit and so is omitted for clarity.

The values of r_A^2 obtained during this work are listed in Table X. The smaller r_A^2 values from the $k_{\max} = 6$ fits are consistent with the extraction of r_A^2 from Ref. [18], which claims $r_A^2 = 0.46(16)$ fm^2 in agreement with this work.

Other historical assessments of r_A^2 appealed to the dipole parametrization for the axial form factor, which does not allow sufficient freedom to describe the form factor shape and leads to underestimated uncertainty. Such works include deuterium scattering and pion electroproduction constraints from Ref. [7], which lists the values $r_A^2 = 0.453(23)$ fm^2 and $r_A^2 = 0.454(14)$ fm^2, respectively, as well as neutrino-carbon scattering from the MiniBooNE experiment [59] with $r_A^2 = 0.26(7)$ fm^2[3] and the NOMAD experiment [60] with $r_A^2 = 0.42(5)$ fm^2. For a comprehensive list of previous axial radius calculations, see Ref. [61].

The result of the fit to the MINERvA hydrogen dataset is significantly higher than the deuterium fit result above $Q^2 \approx 0.25$ GeV^2 and above the fit result from Ref. [8] above $Q^2 \approx 0.6$ GeV^2. However, the value of r_A^2 is consistent between the hydrogen and deuterium datasets. This suggests that the shape of the hydrogen data are not well captured by the dipole parametrization, which would need to follow closely with the result of Ref. [8] to match the same slope at $Q^2 = 0$. This nontrivial shape is possible to describe well with the z expansion parametrization. The agreement between the r_A^2 values also suggests that measurements sensitive to only to low Q^2 behavior of the form factor could not be used to make strong inferences about the form factor shape at higher Q^2.

The quasielastic cross section obtained from the fits in this work are shown in Fig. 12. The Q^2-dependence of the form factors is integrated to produce a total cross section. The slower Q^2 falloff of the LQCD and MINERvA results therefore corresponds to a larger cross section, enhanced by as much as 30%–40% for the LQCD average compared to the deuterium result.

[3]This is computed from an effective axial mass that is obtained by modifying the nuclear binding energy.

TABLE X. Summary of the r_A^2 values obtained from fits in this work for both choices of $k_{\max}$. The MINERvA fit with $k_{\max} = 7$ also imposes the regularization $\lambda = 0.1$, which accounts for the decrease in uncertainty in moving from $k_{\max} = 6$ to $k_{\max} = 7$. Except for the row for deuterium, which sets $\lambda = 1$, all other fits use $\lambda = 0$.

	r_A^2/fm^2		
Fit	$k_{\max} = 6$	$k_{\max} = 7$	Ref. [8]
MINERvA	0.575(222)	0.565(149)	
LQCD	0.369 (30)	0.341 (62)	
Deuterium	0.334(254)	0.434(215)	0.46(22)
MINERvA + LQCD	0.364 (30)	0.408 (55)	

V. DISCUSSION

In this work, neutrino scattering data from multiple elementary target sources are examined to determine the most up-to-date knowledge for the nucleon quasielastic axial form factor. This work appeals to historic deuterium bubble chamber datasets, a recent work by the MINERvA collaboration to extract the antineutrino-hydrogen scattering cross section, and first principles computations with LQCD. This builds upon the previous work of Ref. [8] and was prepared in conjunction with the sister paper, Ref. [17].

There are a number of departures from the results of the previous work of Ref. [8] that are notable. Of these, the most significant is the heuristic used to choose a set of priors for the z expansion coefficients. In Ref. [8], the priors were chosen to satisfy expectations from unitarity

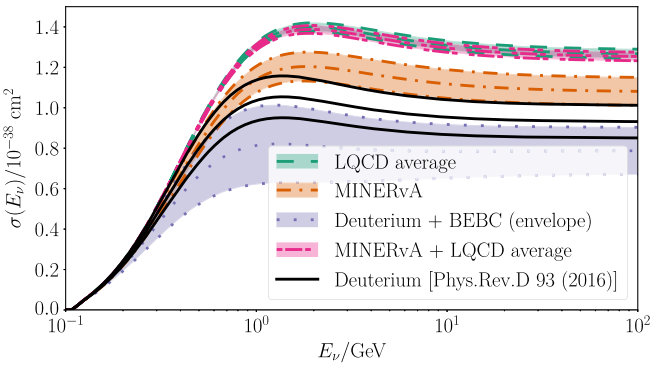


FIG. 12. The quasielastic cross section for the interaction $\nu_\mu n \to \mu^- p$. The cross section assumes the same form factor choices used to perform the fits in this work. For all of the fits, the curves for the central value and $\pm 1\sigma$ uncertainties are shown as three separate lines, with shading between the uncertainty bounds. The deuterium fit (blue-violet dotted) shows the full error envelope of the two $Q^2_{\min}$ cuts. The previous work of Ref. [8] (unfilled solid black) is shown for comparison.

preventing higher-order coefficients from being unnaturally large compared to lower-order coefficients. As a departure from that heuristic, this work uses the relationship between χ^2_{data} and χ^2_{penalty} to choose the point of lowest curvature on an L-curve plot, described in Sec. III A. This corresponds to a compromise between the dependence of the fit coefficients on prior widths versus on the data itself.

Using an L-curve heuristic for choosing prior widths in Sec. III C revealed a degeneracy between the data normalization and form factor shape. The floating normalizations that were applied to overcome the unknown absolute normalization of the neutrino event rates also prevent pinning down the shape of the form factor in the absence of a strong prior. For deuterium fits, the L-curve heuristic in Fig. 2 indicates that a milder prior constraint is preferred by the fits, which exposes the degeneracy that manifests as a strong dependence on the Q^2_{min} cutoff. This degeneracy was not observed in the analysis of Ref. [8] because of the regularization of the z expansion parameters with $\lambda = 1$. This work finds such a strong regularization to be too constraining. The resulting curve is overfit and likely underestimating the uncertainty, much like how the dipole parametrization with only the axial mass as a free parameter historically led to underestimated uncertainties.

Relaxing the regularization term by decreasing $\lambda \to 0$ allows for a large range of variation of the form factor. The effects of the aforementioned degeneracy is partially overcome in this work by introducing the BEBC dataset to the fits, which does have an absolute normalization up to a flux uncertainty and can pin the fits down to within about 2σ of the BEBC central value depending on the Q^2_{min} cut. However, the lack of absolute normalization still leads to substantial systematic uncertainty on the form factor shape. This is not accounted for explicitly in the fits but is schematically represented by an uncertainty envelope in Fig. 10.

If a there were a sufficiently well-motivated systematic that could account for the range of variation exhibited by the deuterium results, inclusion of this would significantly reduce the constraining power of the deuterium data relative to the hydrogen and LQCD. If this were realized, it seems plausible that the deuterium results would be compatible with the MINERvA and LQCD fits.

The compatibility of neutrino scattering datasets was tested with 1 degree of freedom $\Delta\chi^2$ comparisons outlined in Sec. III B. Testing compatibility of the neutrino scattering datasets in Sec. III C shows that the datasets with deuterium targets, including the BEBC result, are consistent with each other but not with the MINERvA hydrogen result. The combined fits including both hydrogen and deuterium are dominated by the deuterium fit results. The minimum preferred by the MINERvA experiment disagrees with the joint-fit minimum (and therefore the deuterium minimum) enough to increase the $\Delta\chi^2$ and fail a compatibility test. Although the compatibility is almost permissible for the $Q^2_{\text{min}} = 0.06$ GeV^2 combined fit, that apparent compatibility is a consequence of the poorly described fit data at low Q^2 that coincidentally push the combined fit result closer to the preferred MINERvA hydrogen minimum.

The key difference between the single-nucleon results, including MINERvA hydrogen and LQCD, versus the deuterium results is the falloff behavior of the form factor with respect to Q^2. The single-nucleon results fall with Q^2 slower than the deuterium results. This was consistently realized in the LQCD results, which first started reporting slow Q^2 falloff as early as 2020 [34–38]. Later corroborating evidence has come not only from the MINERvA [16,49] results explored here, but also Monte Carlo tunes [9,10], generalized parton distributions [62,63], and Schwinger functional methods [64,65].

Given the model assumptions inherent in using a deuterium target, the known efficiency issues at low Q^2, and the lack of historical preservation of the data, the shape tension between the hydrogen and deuterium datasets calls into question the accuracy of the deuterium data. This work has made the choice to omit the deuterium data as a result of these deficiencies. Possible sources of the tension could be the lack of energy transfer-dependence in the deuterium correction, or from growing overlap between the quasielastic and Δ resonance responses at moderate momentum transfers [51]. Even if the deuterium data were still included in the fits, the systematic uncertainty that must be introduced to account for the lack of absolute normalization would decrease the pull of the deuterium data in a combined fit, leaving the fits to be dominated mostly by the LQCD and MINERvA results.

If the slower falloff with Q^2 is born out by future constraints, then this will have substantial impacts for neutrino oscillation analyses. This was demonstrated in Ref. [11] by substituting a representative LQCD result into the GENIE Monte Carlo event generator. Neutrino oscillation experiments would see E_ν-dependent changes to the event rates if the axial form factor is modified from a dipole to the new LQCD average. These observations warrant due caution when tuning to neutrino scattering data and advocate for selection of models that are flexible enough to account for the full range of possible variations.

The parametrizations for all of the fits obtained in this work are listed in Sec. IV, including the fits to the MINERvA dataset, a translation of the results of Ref. [8] to the parameter set used in this work, a summary of the LQCD fit results from Ref. [17], and a combined fit to both MINERvA and LQCD. Under the L-curve heuristic, the MINERvA fit tolerates unregularized fits with $k_{\text{max}} = 6$ as an optimal choice. The LQCD result similarly prefers $k_{\text{max}} = 6$ based on fit p values. The MINERvA dataset alone achieves a fractional uncertainty of 7% at $Q^2 = 0.50$ GeV^2, already indicating an improvement over the precision assumed in Ref. [8]. With LQCD results included,

the precision improves to a 2% fractional uncertainty at $Q^2 = 0.50\ \mathrm{GeV}^2$. At the level of 1% fractional uncertainty, other systematics would become relevant before further improvement could be achieved, such as tensions between vector form factors in Refs. [28,29], or isospin corrections [66].

A. Recommendations for the axial form factor

Based on this work, we recommend replacing the deuterium results by the $k_{\max} = 6$ results for either LQCD or LQCD + MINERvA as the new best form factor parametrization. Given the observed agreement between the MINERvA and the LQCD results, both of which are truly free nucleon constraints on the axial form factor, it appears likely that the deuterium datasets have some systematic effect that is not properly accounted for. This suspicion of the deuterium bubble chamber results, combined with an ill-defined inflation of the uncertainty to account for both $Q^2_{\min}$ cuts, would likely result in the deuterium contributing minimally or contributing misinformation in a combined fit with all data sources.

The MINERvA result achieves a reasonable constraint on the uncertainty, but the constraint from LQCD is significantly more precise and joint fits between the two is dominated by the LQCD.

If one wanted a "theory-free" determination of the axial form-factor, one could simply use the MINERvA result. However, given the consistency between the LQCD and MINERvA result, there is no clear motivation for doing so.

Although both LQCD and MINERvA results fit well to $k_{\max} = 7$ parametrizations, the improvement to χ^2 is not large enough to overcome the decrease to the degrees of freedom, resulting in slightly smaller p values. This suggests that the additional free parameter in the $k_{\max} = 7$ fits is likely not well-informed by the data and is only working to inflate the uncertainty.

B. Future directions

There are several possibilities of future investigation to refine the present work. New neutrino scattering data from hydrogen and deuterium targets will without doubt contribute to strengthen constraints on the shape of the axial form factor. Studies of modern pion electroproduction data, interpreted with the help of appropriately flexible model parametrizations, could provide more information about the low momentum transfer region of the axial form factor and the squared axial radius. Simultaneous fits to the axial and vector form factors together could yield interesting surprises, specifically by leveraging the purely isovector weak interaction to pin down slight degeneracies in the vector form factor contributions. LQCD will also have the same benefit, providing linearly independent constraints on the isospin-symmetric vector form factors and induced pseudoscalar form factor in addition to the axial form factor. In the near future, LQCD could also make headway toward understanding deficiencies in our understanding of deuterium corrections at large energy and momentum transfers by producing explicit matrix element calculations with two-nucleon systems. The availability of both free nucleon and deuteron responses would provide valuable insights about the nature of interactions binding nucleons together into atomic nuclei.

This work has advanced the field another step toward a precise axial form factor parametrization from elementary target sources. Making use of all of available datasets is essential for maximizing the physics potential of upcoming neutrino oscillation experiments. With the high-precision experiments currently running and new flagship experiments just around the corner, supporting theory predictions of neutrino scattering cross sections are of critical importance.

DATA AVAILABILITY

The datasets that support the findings of this article are openly available [49].

ACKNOWLEDGMENTS

The authors would like to thank Sara Collins, Peter Denton, Lukas Koch, Andreas Kronfeld, Sasha Tomalak, André Walker-Loud, Callum Wilkinson, and Clarence Wret for useful discussions. The work of A. S. M. was performed under the auspices of the U.S. Department of Energy by Lawrence Livermore National Laboratory under Contract No. DE-AC52-07NA27344 and the Neutrino Theory Network Program under Grant No. DE-AC02-07CHI11359 and U.S. Department of Energy Award No. DE-SC0020250. The work of R. J. H. was supported by the U.S. Department of Energy, Office of Science, Office of High Energy Physics, under Award No. DE-SC0019095 (R. J. H). Other authors performed this work as members of the MINERvA collaboration, and their work was supported using the resources of the Fermi National Accelerator Laboratory (Fermilab), a U.S. Department of Energy, Office of Science, HEP User Facility. Fermilab is managed by Fermi Research Alliance, LLC (FRA), acting under Contract No. DE-AC02-07CH11359. Support for participating scientists in the MINERvA collaboration was provided by NSF and DOE (USA); by CAPES and CNPq (Brazil); by CoNaCyT (Mexico); by ANID PIA / APOYO AFB180002, CONICYT PIA ACT1413, and Fondecyt 3170845 and 11130133 (Chile); by CONCYTEC (Consejo Nacional de Ciencia, Tecnología e Innovación Tecnológica), DGI-PUCP (Dirección de Gestión de la Investigación—Pontificia Universidad Católica del Peru), and VRI-UNI (Vice-Rectorate for Research of National University of Engineering) (Peru); NCN Opus Grant No. 2016/21/B/ST2/01092 (Poland); by Science and Technology Facilities Council (UK); by EU Horizon 2020

Marie Skłodowska-Curie Action; by a Cottrell Postdoctoral Fellowship from the Research Corporation for Scientific Advancement; by an Imperial College London President's PhD Scholarship.

APPENDIX: IMPLEMENTATION OF SUM RULES

The sum rules in Eqs. (10) and (11) are a linear system of equations that can be solved analytically. The z expansion coefficients are first separated into two categories, namely the coefficients that are fit,

$$a = [a_1, a_2, \ldots, a_{k_{\max}-4}], \tag{A1}$$

and the coefficients that are fixed by sum rule constraints,

$$b = [a_0, a_{k_{\max}-3}, a_{k_{\max}-2}, a_{k_{\max}-1}, a_{k_{\max}}]. \tag{A2}$$

The intercept g_A for the fixed coupling gets its own separate vector,

$$g = [g_A, 0, 0, 0, 0]. \tag{A3}$$

Then the sum rules can be cast as a matrix equation

$$Vb + Wa - g = 0 \tag{A4}$$

with square matrix V of size 5×5 and rectangular matrix W of size $5 \times (k_{\max} - 4)$. Implementation of the sum rules then amounts to solving for b,

$$b = -V^{-1}(Wa - g). \tag{A5}$$

The matrix W has as its elements the prefactors in Eqs. (10) and (11), taking the form

$$W = \begin{pmatrix} z_0 & z_0^2 & z_0^3 & \cdots & z_0^{K-4} \\ 1 & 1 & 1 & \ldots & 1 \\ 1 & 2 & 3 & \ldots & K-4 \\ 0 & 2 & 6 & \ldots & (K-4)(K-5) \\ 0 & 0 & 6 & \ldots & (K-4)(K-5)(K-6) \end{pmatrix} \tag{A6}$$

where $K = k_{\max}$ and $z_0 = z(Q^2 = 0)$ are used to shorten the expressions. The matrix V takes a similar form

$$V = \begin{pmatrix} 1 & z_0^{K-3} & z_0^{K-2} & z_0^{K-1} & z_0^{K} \\ 1 & 1 & 1 & 1 & 1 \\ 0 & K-3 & K-2 & K-1 & K \\ 0 & (K-3)(K-4) & (K-2)(K-3) & (K-1)(K-2) & K(K-1) \\ 0 & (K-3)(K-4)(K-5) & (K-2)(K-3)(K-4) & (K-1)(K-2)(K-3) & K(K-1)(K-2) \end{pmatrix}. \tag{A7}$$

Once the parameters $k_{\max}$, t_c, and t_0 are specified, the elements of the matrices V and W are fixed and may be computed once at the start of a fit.

Writing the inverse as a set of column vectors v_i,

$$V^{-1} = \frac{1}{\Delta}[v_0, v_1, v_2, v_3, v_4] \tag{A8}$$

with

$$\begin{aligned} \Delta = 2z_0^{K-3}[&z_0^3(K-3)(K-2)(K-1) - 3Kz_0^2(K-3)(K-2) \\ &+ 3Kz_0(K-3)(K-1) - K(K-2)(K-1)] + 12, \end{aligned} \tag{A9}$$

the elements of the inverse matrix are

$$v_0 = \begin{pmatrix} -2K(K-2)(K-1) \\ 6K(K-3)(K-1) \\ -6K(K-3)(K-2) \\ 2(K-3)(K-2)(K-1) \\ 12 \end{pmatrix}, \tag{A10}$$

$$v_1 = \begin{pmatrix} 2K(K-2)(K-1) \\ -6K(K-3)(K-1) \\ 6K(K-3)(K-2) \\ -2(K-3)(K-2)(K-1) \\ 2z_0^{K-3}[z_0^3(K-3)(K-2)(K-1) - 3z_0^2K(K-3)(K-2) + 3z_0K(K-3)(K-1) - K(K-2)(K-1)] \end{pmatrix}, \quad \text{(A11)}$$

$$v_2 = \begin{pmatrix} -6(K-2)(K-1) + z_0^{K-2}(K-2)(K-1)[z_0^2(K-3)(K-2) - 2z_0K(K-3) + K(K-1)] \\ 6(K-1)(3K-8) - (K-1)z_0^{K-3}[2z_0^3(K-4)(K-3)(K-2) - 3z_0^2K(K-4)(K-3) + K(K-2)(K-1)] \\ -6(K-3)(3K-4) + (K-3)z_0^{K-3}[z_0^3(K-4)(K-3)(K-2) - 3z_0K(K-4)(K-1) + 2K(K-2)(K-1)] \\ 6(K-3)(K-2) - (K-3)(K-2)z_0^{K-3}[z_0^2(K-4)(K-3) - 2z_0(K-4)(K-1) + (K-2)(K-1)] \\ -6z_0^{K-3}(z_0-1)[z_0^2(K-3)(K-2) - 2z_0(K-3)(K-1) + (K-2)(K-1)] \end{pmatrix}, \quad \text{(A12)}$$

$$v_3 = \begin{pmatrix} 6(K-2) - 2(K-2)z_0^{K-2}[z_0^2(K-3)(K-1) - z_0K(2K-5) + K(K-1)] \\ -6(3K-7) + z_0^{K-3}[2z_0^3(K-3)(K-1)(2K-7) - 6z_0^2K(K-3)^2 + 2K(K-2)(K-1)] \\ 6(3K-8) + z_0^{K-3}[-2z_0^3(K-4)(K-3)(K-2) + 6z_0K(K-3)^2 - 2K(K-2)(2K-5)] \\ -6(K-3) + 2(K-3)z_0^{K-3}[z_0^2(K-4)(K-2) - z_0(K-1)(2K-7) + (K-2)(K-1)] \\ 6z_0^{K-3}(z_0-1)^2(z_0(K-3) - (K-2)) \end{pmatrix}, \quad \text{(A13)}$$

and

$$v_4 = \begin{pmatrix} -2 + z_0^{K-2}[z_0^2(K-2)(K-1) - 2z_0K(K-2) + K(K-1)] \\ 6 - z_0^{K-3}[2z_0^3(K-3)(K-1) - 3z_0^2K(K-3) + K(K-1)] \\ -6 + z_0^{K-3}[z_0^3(K-3)(K-2) - 3z_0K(K-3) + 2K(K-2)] \\ 2 - z_0^{K-3}[z_0^2(K-3)(K-2) - 2z_0(K-3)(K-1) + (K-2)(K-1)] \\ -2z_0^{K-3}(z_0-1)^3 \end{pmatrix}. \quad \text{(A14)}$$

[1] D. S. Ayres *et al.* (NOvA Collaboration), The NOvA Technical Design Report (unpublished).
[2] Z. Djurcic *et al.* (JUNO Collaboration), arXiv:1508.07166.
[3] R. Acciarri *et al.* (DUNE Collaboration), arXiv:1512.06148.
[4] K. Abe *et al.* (Hyper-Kamiokande Collaboration), arXiv:1805.04163.
[5] B. Abi *et al.* (DUNE Collaboration), arXiv:2002.03005.
[6] V. Bernard, L. Elouadrhiri, and U.-G. Meissner, J. Phys. G **28**, R1 (2002).
[7] A. Bodek, S. Avvakumov, R. Bradford, and H. S. Budd, Eur. Phys. J. C **53**, 349 (2008).
[8] A. S. Meyer, M. Betancourt, R. Gran, and R. J. Hill, Phys. Rev. D **93**, 113015 (2016).
[9] P. Abratenko *et al.* (MicroBooNE Collaboration), Phys. Rev. D **105**, 072001 (2022).
[10] J. Tena-Vidal *et al.* (GENIE Collaboration), Phys. Rev. D **106**, 112001 (2022).
[11] A. S. Meyer, A. Walker-Loud, and C. Wilkinson, Annu. Rev. Nucl. Part. Sci. **72**, 205 (2022).
[12] O. Tomalak, R. Gupta, and T. Bhattacharya, Phys. Rev. D **108**, 074514 (2023).
[13] H. Wachsmuth, Neutrino and muon fluxes in the CERN 400-geV proton beam dump experiments, Ph.D. thesis, European Organization for Nuclear Research, 1979.
[14] S. J. M. Barlag, Quasi-elastic interactions and one-pion production by neutrinos and anti-neutrinos on a deuterium target, Ph.D. thesis, Nationaal Instituut voor Kernfysica en Hoge Energy Fysica, 1984.
[15] D. Allasia *et al.*, Nucl. Phys. **B343**, 285 (1990).
[16] T. Cai *et al.* (MINERvA Collaboration), Nature (London) **614**, 48 (2023).

[17] A. S. Meyer, arXiv:2601.02676.
[18] R. J. Hill, P. Kammel, W. J. Marciano, and A. Sirlin, Rep. Prog. Phys. **81**, 096301 (2018).
[19] V. Bernard, N. Kaiser, and U. G. Meissner, Phys. Rev. Lett. **69**, 1877 (1992).
[20] K. I. Blomqvist *et al.*, Z. Phys. A **353**, 415 (1996).
[21] A. Liesenfeld *et al.* (A1 Collaboration), Phys. Lett. B **468**, 20 (1999).
[22] M. Hilt, B. C. Lehnhart, S. Scherer, and L. Tiator, Phys. Rev. C **88**, 055207 (2013).
[23] A. Czarnecki, W. J. Marciano, and A. Sirlin, Phys. Rev. Lett. **99**, 032003 (2007).
[24] V. A. Andreev *et al.* (MuCap Collaboration), Phys. Rev. Lett. **110**, 012504 (2013).
[25] V. A. Andreev *et al.* (MuCap Collaboration), Phys. Rev. C **91**, 055502 (2015).
[26] C. H. Llewellyn Smith, Phys. Rep. **3**, 261 (1972).
[27] J. A. Formaggio and G. P. Zeller, Rev. Mod. Phys. **84**, 1307 (2012).
[28] R. Bradford, A. Bodek, H. S. Budd, and J. Arrington, Nucl. Phys. B, Proc. Suppl. **159**, 127 (2006).
[29] K. Borah, R. J. Hill, G. Lee, and O. Tomalak, Phys. Rev. D **102**, 074012 (2020).
[30] Z. Ye, J. Arrington, R. J. Hill, and G. Lee, Phys. Lett. B **777**, 8 (2018).
[31] S. L. Adler, Phys. Rev. **137**, B1022 (1965).
[32] S. L. Adler, Phys. Rev. **139**, B1638 (1965).
[33] Y.-C. Jang, R. Gupta, B. Yoon, and T. Bhattacharya, Phys. Rev. Lett. **124**, 072002 (2020).
[34] G. S. Bali, L. Barca, S. Collins, M. Gruber, M. Löffler, A. Schäfer, W. Söldner, P. Wein, S. Weishäupl, and T. Wurm (RQCD Collaboration), J. High Energy Phys. 05 (2020) 126.
[35] S. Park, R. Gupta, B. Yoon, S. Mondal, T. Bhattacharya, Y.-C. Jang, B. Joó, and F. Winter (Nucleon Matrix Elements (NME) Collaboration), Phys. Rev. D **105**, 054505 (2022).
[36] D. Djukanovic, G. von Hippel, J. Koponen, H. B. Meyer, K. Ottnad, T. Schulz, and H. Wittig, Phys. Rev. D **106**, 074503 (2022).
[37] Y.-C. Jang, R. Gupta, T. Bhattacharya, B. Yoon, and H.-W. Lin (Precision Neutron Decay Matrix Elements (PNDME) Collaboration), Phys. Rev. D **109**, 014503 (2024).
[38] C. Alexandrou, S. Bacchio, M. Constantinou, J. Finkenrath, R. Frezzotti, B. Kostrzewa, G. Koutsou, G. Spanoudes, and C. Urbach, Proc. Sci. LATTICE2024 (**2025**) 330. [arXiv:2502.07583].
[39] R. J. Hill and G. Paz, Phys. Rev. D **82**, 113005 (2010).
[40] B. Bhattacharya, R. J. Hill, and G. Paz, Phys. Rev. D **84**, 073006 (2011).
[41] S. Navas *et al.* (Particle Data Group Collaboration), Phys. Rev. D **110**, 030001 (2024).
[42] See Supplemental Material at http://link.aps.org/supplemental/10.1103/ptwr-t73j for more details.
[43] W. A. Mann *et al.*, Phys. Rev. Lett. **31**, 844 (1973).
[44] S. J. Barish *et al.*, Phys. Rev. D **16**, 3103 (1977).
[45] S. J. Barish *et al.*, Phys. Rev. D **19**, 2521 (1979).
[46] K. L. Miller *et al.*, Phys. Rev. D **26**, 537 (1982).
[47] N. J. Baker, A. M. Cnops, P. L. Connolly, S. A. Kahn, H. G. Kirk, M. J. Murtagh, R. B. Palmer, N. P. Samios, and M. Tanaka, Phys. Rev. D **23**, 2499 (1981).
[48] T. Kitagaki *et al.*, Phys. Rev. D **28**, 436 (1983).
[49] L. Zazueta *et al.* (MINERvA Collaboration), Phys. Rev. D **107**, 012001 (2023).
[50] S. K. Singh, Nucl. Phys. **B36**, 419 (1972).
[51] G. Shen, L. E. Marcucci, J. Carlson, S. Gandolfi, and R. Schiavilla, Phys. Rev. C **86**, 035503 (2012).
[52] P. C. Hansen, SIAM Rev. **34**, 561 (1992).
[53] P. C. Hansen, *The l-Curve and Its Use in the Numerical Treatment of Inverse Problems* (WIT Press, United Kingdom, 2001), pp. 119–142.
[54] L. Hulthén, Ark. Mat. Astron. Fys. **28** (1942).
[55] L. Hulthén, Ark. Mat. Astron. Fys. B **29** (1942).
[56] L. Hulthén and M. Sugawara, The two-nucleon problem, in *Structure of Atomic Nuclei / Bau der Atomkerne* (Springer, Berlin, Heidelberg, 1957), pp. 1–143.
[57] L. Koch, Phys. Rev. D **111**, 033002 (2025).
[58] J. E. Amaro and E. Ruiz Arriola, Phys. Rev. D **93**, 053002 (2016).
[59] A. A. Aguilar-Arevalo *et al.* (MiniBooNE Collaboration), Phys. Rev. D **81**, 092005 (2010).
[60] V. Lyubushkin *et al.* (NOMAD Collaboration), Eur. Phys. J. C **63**, 355 (2009).
[61] M. Goharipour, F. Irani, M. H. Amiri, H. Fatehi, B. Falahi, A. Moradi, and K. Azizi (MMGPDs Collaboration), Nucl. Phys. **B1017**, 116962 (2025).
[62] H. Hashamipour, M. Goharipour, and S. S. Gousheh, Phys. Rev. D **100**, 016001 (2019).
[63] F. Irani, M. Goharipour, H. Hashamipour, and K. Azizi, Phys. Rev. D **108**, 074018 (2023).
[64] C. Chen, C. S. Fischer, C. D. Roberts, and J. Segovia, Phys. Rev. D **105**, 094022 (2022).
[65] C. Chen and C. D. Roberts, Eur. Phys. J. A **58**, 206 (2022).
[66] V. Cirigliano, J. de Vries, L. Hayen, E. Mereghetti, and A. Walker-Loud, Phys. Rev. Lett. **129**, 121801 (2022).